Experimental and mathematical insights on the interactions between poliovirus and a defective interfering genome

Yuta Shirogane[1,2†], Elsa Rousseau[3,4†], Jakub Voznica[1,5†], Yinghong Xiao[1] , Weiheng Su[1], Adam Catching[1] , Zachary J.Whitfield[1], Igor M. Rouzine[1,6], Simone Bianco[3,4*], Raul Andino[1*]

[1] Department of Microbiology and Immunology, University of California, San Francisco, San Francisco, CA 94158, USA

[2] Department of Virology, Faculty of Medicine, Kyushu University, Fukuoka, 812-8582, Japan

[3] Department of Industrial and Applied Genomics, AI and Cognitive Software Division, IBM Almaden Research Center, 650 Harry Road, San Jose, CA 95120-6099, USA

[4] NSF Center for Cellular Construction, University of California, San Francisco, San Francisco, CA 94158, USA

[5] ENS Cachan, Université Paris-Saclay, 61 Avenue du Président Wilson, Cachan, 94230, France

[6] UMR 7238 CNRS, Université Pierre et Marie Curie, Institut de Biologie Paris Seine, France

[7] National Engineering Laboratory for AIDS Vaccine, School of Life Sciences, Jilin University, Changchun 130012, China

* Corresponding authors: raul.andino@ucsf.edu (RA), sbianco@us.ibm.com (SB)

†These authors contributed equally to this work

1 Abstract

During replication, RNA viruses accumulate genome alterations, such as mutations and deletions. The interactions between individual variants can determine the fitness of the virus population and, thus, the outcome of infection. To investigate the effects of defective interfering genomes (DI) on wild-type (WT) poliovirus replication, we developed an ordinary differential equation model. We experimentally determined virus and DI replication during co-infection, and use these data to infer model parameters. Our model predicts, and our experimental measurements confirm, that DI replication and encapsidation are the most important determinants for the outcome of the competition. WT replication inversely correlates with DI replication. Our model predicts that genome replication and effective DI genome encapsidation are critical to effectively inhibit WT production, but an equilibrium can be established which enables WT to replicate, albeit to reduce levels.

2 Introduction

Co-infections, the simultaneous infection of a host by multiple pathogen species, are frequently observed [1, 2]. The interactions between these microrganisms can determine the trajectories and outcomes of infection. Indeed, competition between pathogen species or strains is a major force driving the composition, dynamics and evolution of such populations [1, 3]. Three types of competition among free-living organisms have been defined from an ecological point of view: exploitation, apparent and interference competition [1–3]. Exploitation competition is a passive process in which pathogens compete for access to host resources. Apparent competition is competition that is not due to using shared resources, but to having a predator in common [4], and is generally associated with the stimulation of host immune response [3]. Interference competition represents a direct attack inhibiting the growth, reproduction or transmission of competitors, either chemically or mechanically [5].

Here we focus on the interference competition between two RNA virus genomes co-infecting a single cell, one being a fully operational wild-type (WT) poliovirus type 1 (PV1) and the other a defective replicon of PV1, lacking the region encoding for capsid proteins, and called a defective interfering (DI) genome. Poliovirus, the causative agent of

poliomyelitis, is a positive-sense single-stranded RNA enterovirus belonging to the family *Picornaviridae* [6]. Upon cell infection, WT poliovirus initiates a series of processes that leads to the production of structural and nonstructural viral proteins and genome amplification. Structural proteins encapsidate the viral RNA, which leads to infectious viral particle production and cell-to-cell spread. Indeed, only encapsidated poliovirus genomes can survive outside the cells and can bind to new cells to initiate infections.

As an RNA virus, poliovirus is characterized by a high level of genome plasticity and evolution capacity, due to both high replication rate and error-prone nature of viral RNA polymerase [7, 8], which generates a large proportion of mutants in the viral population, called viral quasispecies [9–11]. In addition, defective genomes, lacking essential genes, are produced by defective replication or viral RNA recombination [12–14]. Natural poliovirus DI particles have been observed with in-frame deletion in the P1 region of the genome encoding structural capsid proteins, while expression of nonstructural proteins is not affected [15, 16]. The DI genome used in this study features similar deletion of the P1 region. When co-infecting a cell with the WT, it can exploit capsid proteins produced by the WT to form DI particles, and in this way spread to new cells. However, it is not able to reproduce when not co-infecting a cell with the WT helper virus [16].

From an ecological perspective, the WT can be viewed as a cooperator, producing capsid proteins as public goods. The DI particles are non-producing cheaters, bearing no production cost while exploiting the capsid protein products from the WT [1, 3]. Hence, co-infection should enable DI particles to replicate and spread, while hindering WT growth and propagation by interference competition.

DI particles have been reported for a large number of viral species, such as vesicular stomatitis virus [17], poliovirus [18], ebola virus [19], dengue virus [20] or influenza virus [21, 22]. Given that DI particles hamper WT production, they can attenuate WT virus infection [18, 22]. A recent study showed that defective viral genomes can contribute to attenuation in influenza virus infected patients [23], and they can protect from experimental challenges with a number of pathogenic respiratory viruses [24, 25].

In this study, we examined the competition between poliovirus WT and DI genomes within cells during one infection cycle. We then developed an ordinary differential equations (ODEs) mathematical model that capture the dynamics of DI and WT replication and encapsidation. We aimed to understand the mechanisms of interference of the de-

fective genome with WT within a cell. Our study indicates that DI and WT genomes compete for limiting cellular resources required for their genome amplification and for capsid proteins required for particle morphogenesis. The model was further used to evaluate the potential outcome of the interaction between DIs and WT viruses over a large range of parameter values and initial conditions (multiplicities of infection, temporal spacing and order of infection). As a result we identified the most important parameters affecting WT production by DI co-infection. DI particles are spontaneously generated during a significant number of virus infection, but the factors affecting DIs generation and propagation are not well understood. Our mathematical and experimental results indicate that DIs compete at two different steps during poliovirus cycle. This competition affects virus production and the outcome of infection. Thus, the mathematical model described facilitate the understanding and interpretation of the biological impact of DI particles in the context of virus infection.

3 Results

3.1 Interference of WT poliovirus production by DI genomes

Initially, we evaluated whether DI genomes, carrying a deletion of the entire region encoding for capsid proteins, could affect progression of WT virus infection (Fig 1A). The DI genome used in this study does not produce capsid proteins and is thus unable to encapsidate its genome and spread to other cells. However, it retains full capacity to produce nonstructural viral proteins and replicate its genomic RNA. WT poliovirus and DI genomic RNAs were transfected by electroporation to HeLaS3 cells and infectious titers of WT virus were determined over time by plaque assay (see Material and Methods). As a control we also evaluated a replication-incompetent defective RNA lacking the capsid-encoding region, a part of 3D-polymerase encoding region, and the entire 3' non-translated region (NTR). HeLaS3 cells transfected by only WT genomes produced nearly 1×10^7 PFU/ml WT virus 9 hours after transfection, while co-transfection of WT genomes together with DI RNAs at a ratio WT:DI=1:4 resulted in 100-fold decrease of WT titers (Fig 1B). The non-replicating defective RNA did not affect WT virus production, suggesting that replicating DI genomes are required for effective interference, as previously reported [26].

3.2 Quantification of the copy number of WT and DI genomes following co-transfection

Next, we examined the interaction between DI and WT genomes by varying the ratio of each RNA used to initiate transfection. Starting with equal RNA concentrations (5μg) DI genomes were 4 times more efficiently transfected than WT (data not shown). Given that DI genomes are ~2,000 nucleotide shorter (~1/4 shorter) than WT genomes, the copy number of DI genomes are higher than that of WT genomes and transfection of shorter genomes is also more efficient than larger RNAs. We optimized our protocol to deliver equal copy number of DI and WT genomes into the transfected cells. We transfected 5μg of WT to 1.25μg of DI genomes, and we collected RNA samples at given timepoints (t=0, 2, 3.5, 5, 7 and 9 hours after transfection). The average number of genomes in a single cell was estimated as the total number of genomes divided by the number of transfected cells. Replication rates of WT and DI decreased ~7 hours after co-transfection, but this effect was not observed in the cells transfected only with WT or DI (Fig 1C). Thus, replication of WT genomes was inhibited by DI genomes, and the number of accumulated DI also decreased in the presence of WT. This suggests that WT and DI genomes compete for a limiting factor for replication. Nonetheless, DI genomes replicated faster than WT genomes (Fig 1C). To determine the numbers of encapsidated WT and DI genomes, we also treated cell lysates with a mixture of RNase A and RNase T1. Viral RNAs encapsidated in virus particles are resistant to RNase activity, while naked RNAs are degraded by RNase-treatment. The decrease of encapsidated WT genomes between singly and dually transfected cells conditions was two-fold larger than that of WT genomes without RNase-treatment, indicating that DI genomes hamper WT genome encapsidation (Fig 1C&D, compare the difference between plain and dashed blue lines at 9 hours after transfection in Fig 1D*i* to the difference in Fig 1C*i*).

Thus, these results are consistent with the idea that DI RNAs replicate faster than WT genomes, due to their shorter genome [27, 28]. Interestingly, co-transfection results in a net reduction in replication of both WT and DI genomes most likely due to competition for some host-cell limiting factor needed for genome amplification. In addition, capsid proteins produced by WT genomes limit DI and WT virus production as DI genomes compete for these proteins and thus further inhibit WT production. To further examine the mechanism of defective interference and quantitatively evaluate the effect of co-replicating DIs,

we designed a simple mathematical model that describes the DI/WT genome interactions.

3.3 Mathematical description of intracellular competition

A deterministic mathematical model describing the intracellular competition between DI and WT genomes was developed, adapted from an existing competition model for human immunodeficiency virus (HIV) [29]. In order to describe appropriately the intracellular dynamics of poliovirus, we explicitly account for limiting resources depleted by the virus during replication, slowing down the growth of the population over time. This slowdown was experimentally shown by [30], who reported an exponential growth of viral RNA up to the third hour of infection, followed by a linear increase and then a plateau. The effect of limiting resources on poliovirus replication has been investigated by [31] using a mathematical model to explain the observed saturation in viral replication dynamics. Resources depleted by the virus may include phospholipids and *de novo* synthesized membranes for the formation of replication organelles [32, 33], host factors regulating viral replication [34], or, as theoretically hypothesized, the number of ribosome complexes available for translation, the supply of amino acids for building proteins or the supply of nucleotides [31]. Our model considers a generic set of resources (R) at the virus disposal during replication. It describes the changes, over the course of infection of a cell, of the numbers of WT (G_{WT}) and DI (G_{DI}) positive-sense RNA genome copies, of free capsids produced by the WT (C) and of limiting resource units (R) depleted by the genomes for their replication. The set of ODEs is the following:

$$\frac{dG_{WT}}{dt} = \theta\varepsilon G_{WT}R - c_g\kappa C G_{WT} - \alpha G_{WT} \quad (1)$$

$$\frac{dC}{dt} = \eta\theta\varepsilon G_{WT}R - \kappa(G_{WT} + \omega G_{DI})C - \beta C \quad (2)$$

$$\frac{dG_{DI}}{dt} = P\theta\varepsilon G_{DI}R - \omega c_g\kappa C G_{DI} - \alpha G_{DI} \quad (3)$$

$$\frac{dR}{dt} = \lambda - c_r\varepsilon(G_{WT} + G_{DI})R - \gamma R \qquad R(0) = \lambda/\gamma \quad (4)$$

Model parameters are summarized in Tab 1 and can be described through three distinct stages of the viral cycle: replication, capsid synthesis and encapsidation. A flow diagram of the model is available in Fig 2. Limiting resources are produced at a linear rate λ and

captured by WT (G_{WT}) and DI (G_{DI}) genomes at a rate ε per unit of resource (uor) per minute. One uor and one viral genome, by definition, form one replication complex ($c_r = 1$ uor $\cdot$ genome^{-1}, [35]). Conditionally on the capture of a resource unit, a WT genome replicates and turns into θ genomes, before the replication complex disintegrates (we set the condition $\theta > 1$ in order for virus genomes to replicate). We assume that this happens quickly compared to the other processes. DI genomes replicate faster than WT genomes by a fixed factor P ($P > 1$), which can be related to the smaller genome size of the DI [27, 28]. The replication rate represents an average over the three main steps of poliovirus replication: (i) translation of the positive-sense RNA genome [36], (ii) transcription into negative-sense RNA genome that will be used as template for (iii) transcription into new positive-sense RNA genomes [31, 37]. Because DI genomes lack the genes responsible for capsid proteins synthesis, only WT genomes are capable of producing free capsids (C), with the capsid-to-genome accumulation ratio η. WT genomes are then encapsidated (i.e. packaged into free capsids) at rate κ. DI genomes are assumed to encapsidate faster by a fixed factor ω ($\omega > 1$). One viral genome encapsidates into one capsid to form a virion ($c_g = 1$ genome $\cdot$ capsid^{-1}). Finally, α, β, and γ represent the decay rates of, respectively, viral genomes, free capsids and resources.

The number of encapsidated WT genomes (i.e. WT virions, C_{WT}) and DI genomes (i.e. DI virions, C_{DI}) were measured experimentally (Fig 1D) and can easily be derived from eq 2 as the loss of free capsids due to encapsidation:

$$\frac{dC_{WT}}{dt} = \kappa C G_{WT} \tag{5}$$

$$\frac{dC_{DI}}{dt} = \omega \kappa C G_{DI} \tag{6}$$

Further, burst sizes, which are defined as the number of virions at cell lysis, i.e. 9 hours post transfection (hpt, [38, 39]), can be written as $\mathcal{B}_{WT} = C_{WT}(9 \text{ hpt})$ for WT virions and $\mathcal{B}_{DI} = C_{DI}(9 \text{ hpt})$ for DI virions.

The system of equations 1– 6 encompasses 10 parameters and six variables, among which only four variables could be experimentally measured. Therefore, the mathematical model presents a classical problem of parameter identifiability, specifically regarding parameters ε and θ that appear as a product, with parameter ε figuring separately in Eq. (4) corre-

sponding to the unmeasured variable R. To solve this problem, we built a reduced model by assuming that the decrease in resources due to viral uptake follows a logistic decreasing function. We use a two-step optimization procedure to estimate the parameters. Briefly, we first estimate a set of parameters using the reduced model. Then, we use the parameters that are common between the reduced and the full models as "best guess" and run the estimation on the full model. Using this procedure, we are able to estimate the model parameters with reasonably high confidence (see Material and Methods and Tab 1).
We additionally conducted a model selection procedure in order to validate that the features introduced in our model were improving fitting statistics chosen as (i) the R-squared between experimental and fitted data, and (ii) the log-likelihood and (iii) Akaike information criterion (AIC) of a linear model explaining the experimental data with the fitted data. The different versions of the model that were tested are detailed in Supplementary Methods and the results are presented in Tab S1. In what follows we will present results from both the reduced and full models for comparison. We report a full comparison of the models in the Supplementary Information.

Model predictions fit well the experimental measurements in Fig 1 C&D, with best $R^2 = 0.974$ for the reduced model and 0.965 for the full model (Fig 3). In dually transfected cells, both versions of the model reproduce well the number of naked and encapsidated genome copies. In singly transfected cells, the reduced model somewhat underestimates the number of naked genome copies while fitting satisfactorily the number of encapsidated genome copies. Conversely, the full model describes well the number of naked genome copies but overestimates the number of encapsidated genome copies. Overall, either model is able to capture the lower genome production when WT and DI are co-transfected in a cell as compared to singly transfected cells (compare same color plain or dashed curves between Fig 3A & B). We hypothesized that this effect is the consequence of competing for limiting resources necessary for replication. The model also reproduces the fact that the WT is more hindered by this competition for resources than the DI (Fig 3 A, compare red and blue plain curves) thanks to the higher replication rate of DI genomes ($P = 1.075$, Tab 1). Predictions also demonstrate that DI genomes are more efficiently encapsidated than WT genomic RNA (Fig 3C, compare red and blue plain curves), thanks to the higher encapsidation rate of DI genomes ($\omega = 2.185$, Tab 1). Most importantly, the model is able to describe the decrease in WT encapsidated genomes in dual transfection compared

to single WT transfections (compare Fig 3C & D, blue curves). Thus, it predicts a strong interference between DI and WT.

All parameter estimates are narrowly defined by the fitting procedure (Tab 1) except for θ, λ and γ as they tend to correlate with each other, yielding non-uniqueness of best-fit parameter values (Fig S1A,C-D, see also the distribution of ε values in Fig S1B). Also, a strong log-to-log relationship was found between the resource production to decay ratio λ/γ and the replication factor θ (Fig S1E).
Both the reduced and full models feature a time-dependent virus replication rate (Fig S1F). In the reduced model, this is given by the logistic function $\Lambda(t)$ (Eq 10 in Material and Methods), and in the full model by the product $\theta\varepsilon R(t)$. In both models, the best fit yields approximately the same time-dependent replication rate, starting at $3.07 \cdot 10^{-2}$ for the reduced model and at $3.02 \cdot 10^{-2}$ ($\theta\varepsilon\lambda/\gamma$) for the full model, and decreasing with time towards 0. According to the reduced model, the time of half-decay is 318 minutes (t_0 in Tab 1), which corresponds to 5.3 hours post transfection.

The predictive power of the full model with best estimated parameter values was tested on independent experimental measurements of WT burst size corresponding to various initial DI-to-WT ratios for which the model had not been trained (Fig S2). Relative experimental and predicted WT burst sizes were normalized by their respective value for WT-only transfection. The model was able to predict experimental outputs fairly well, albeit underestimating WT output for some DI-to-WT input ratios. The largest underestimation was observed for the DI-to-WT input ratio of 0.5, and this discrepancy vanished as the input ratio increased.

3.4 Model predictions

The aim of our work is to understand the competition dynamics of WT and DI genomes during co-infection. To achieve this goal, we used the model described above to study how changes in parameter values around their experimental estimates can impact the outcome of the competition. Additionally, we also used the model to evaluate the effect of initial infection conditions, such as initial genome copy numbers of WT and DI and a time delay of cell infection on their respective burst sizes.

3.4.1 Sensitivity analysis

A sensitivity analysis was performed to identify parameters that have a significant effect on the output variable of interest, which we set as the proportion of WT virions at the time of cell lysis, Φ_{WT} (Eq 12). Parameters were varied by $\pm 50\%$ of their best fit value based on experimental data, with five equally spaced values for each parameter (Table 1). The decay rate of genomes was not varied, because it was estimated to be negligible. The results indicate that the DI-to-WT replication ratio, P, and the DI-to-WT encapsidation ratio, ω, as well as their second-order interaction, were the most influential factors for the variation of Φ_{WT}, explaining 76%, 17% and 7% of the variance, respectively (Fig 4A). All the remaining factors and their second-order interactions had a negligible effect (less than 1% of the variance). Hence, our model predicts that only parameters associated with the DI design have a strong impact on the degree of suppression of WT by DI.

To further examine the effect of P and ω, we varied both parameters from their best estimated value (Fig 4B). As expected from the global sensitivity analysis, P was found to be more important than ω for the production of WT virions, the gradient of Φ_{WT} being steeper along P-axis than along ω-axis. Within the tested range of parameters P and ω, the value of Φ_{WT} varied between 2% and 50%. The reference value of Φ_{WT} corresponding to best-fit parameter estimates from experimental data was 23%. Therefore, we can predict that a DI particle with a lower replication factor, or, to a lesser extent, with a lower encapsidation rate than the DI particle used in the present work would weaken its competitivity with the WT virus, potentially leading to an increase in the proportion of WT virions at cell lysis of up to 27%. Conversely, a DI particle characterized by a higher replication factor or a higher encapsidation rate would strengthen its competitivity, potentially leading to a decrease in Φ_{WT} of up to 21%.

3.4.2 Validation of model predictions using DI variants

To evaluate predictions of the model, we next investigated the competition between WT virus and DI variants. Our sensitivity analysis provides a quantitative prediction of the WT/DI competition outcome as a function of the replication fitness of the DIs. As assessed in the previous Section, the most significant determinants for the outcome of infection are the ratio between DI and WT replication, P, and the DI-to-WT encapsidation ratio, ω. To validate these predictions we isolated DI variants with defined replication fitness.

Briefly, DI and WT poliovirus type 3 (PV3) were serially passaged for 8 times (Fig. 5A, Supplementary Methods). We determined PV3 and DIP titers at each passage to gain information on the dynamics of the co-infection experiments (Fig. 5B). Both DI and PV3 compete with each other, which results in a reduction of about 10-folds PV3 titer, and the establishment of an equilibrium in which both PV3 and DIs are maintained for 8 passages (Fig. 5B, red and green squares).

These experiments also serve to determine whether mutations accumulate during co-passaging in either DI or PV3 genomes. This information was used to construct DI particles with defined replication fitness with respect to the original DI (DI Ori). No change in encapsidation efficiency is expected. The mutation rates in RNA viruses can range from 10^{-4} to 10^{-6} per base, while conventional next-generation sequencing (NGS) can only detect variants at a frequency of about 1 in 100-500 (due to sequencing errors). Consequently, many variants in a viral population which exist at low frequencies cannot be distinguished from noise using conventional NGS. Therefore, we used Circular sequencing (CirSeq), a technique developed to improve accuracy of NGS [40, 41]. We engineered several of the mutations identified into the DI cDNA, which facilitates identification of rare variants detection in the population. We identified eight mutations positively selected over passages (Fig. 5C).

To determine the outcome of competition between WT virus and DI mutants HeLaS3 cells were co-transfected with WT poliovirus and DI variants. We then estimated the ratio of DI-to-WT genome copies by RT-PCR over the course of infection (Fig. 5D and Supplementary Methods). In this way we were able to determine P and we established that the model prediction P and the experimental determined WT/DI ratios correlate with a Pearson coefficient of 0.95 (Fig. 5E and F).

3.4.3 Effect of the multiplicity of infection and the timing of co-infection on WT burst size

We use our model to investigate the impact of varying initial conditions including (i) the time difference between WT and DI infection of the cell and (ii) the initial quantities of WT and DI on the WT and DI burst sizes, $\mathcal{B}_{WT}$ and $\mathcal{B}_{DI}$, respectively. First, the time for DI infection compared to WT was varied from -7 to +7 hours post WT virus infection (Fig 6A). Negative delay values indicate that DI infects first, while positive values indicate that

WT infects first. WT was allowed to produce at least one virion at cell lysis when DI was infecting the cell no more than 1.37 hours prior to the WT virus (delay = −1.37 hours). From this delay value, WT burst size increased as a steep logistic function, reaching a plateau at $\mathcal{B}_{WT} = 811$ from a delay for DI infection of around 4 hours post WT infection. The curve of DI burst size was bell-shaped, reaching a maximum of $\mathcal{B}_{DI} = 298$ at a delay for DI infection of 0.4 hours post WT infection. The delay window allowing DI genome to be encapsidated and produce at least 1 virion is narrow, from -3.43 to 4.37 hours. Most importantly, DI burst size superseded WT burst size only until the delay of 0.62 hours. The difference between DI and WT burst sizes was the largest when DI infected the cell 0.03 hours prior to WT ($\mathcal{B}_{DI} - \mathcal{B}_{WT} = 181$).

We then investigated the impact of varying initial WT and DI multiplicities of infection (MOIs, corresponding to the number of viral genomes successfully entering a cell and initiating infection) from 0 to 1000 on WT and DI relative burst sizes (Fig 6B-C). WT burst sizes were normalized by WT burst size obtained for WT:DI = 1:0 MOIs, while DI burst sizes were normalized by DI burst size obtained for WT:DI = 1:1 MOIs. WT relative burst size varied from 0 to 1.11 depending on MOIs. DI relative burst size ranged from 0 to 1.26.

At the optimal initial conditions maximizing WT burst size, WT must infect the cell with a larger MOI than DI. On the other hand, the optimal initial conditions for maximizing DI burst size are when WT is initially present in slightly larger quantity than DI. The DI needs enough WT to exploit its capsids and produce virions. Because (i) the DI replicates and encapsidates faster than the WT, (ii) only the WT produces free capsids and (iii) replication and capsid production result in resource depletion, it is more optimal for DI virion production to have the WT infect a cell in slightly higher quantity than the DI. In that case, the WT has a slight initial advantage over the DI and can use resources to produce free capsids. In return, the DI can exploit those free capsids at its own advantage as it replicates and encapsidates more efficiently.

We also examined the cross-effect of the time delay and the variation of initial MOIs (Fig S4A). Globally, the shapes of WT and DI burst size curves as a function of delay are very similar between different WT and DI MOIs. The observed effect is a shift of the curves on the delay axis. Equal WT and DI MOIs generate very similar WT and DI burst size curves as a function of delay time. At these equal MOIs, DI competes more efficiently

than WT upon co-infection, i.e. simultaneous infection of the cell by DI and WT (Fig S4A,B) and maximal DI burst size occurs when DI infects the cell around 0.3-0.5 hours after the WT (Fig S4A). As WT MOI gets larger than DI MOI, both the delay time that maximizes the DI to WT burst size difference and the peak of DI burst size shift towards delays where DI infects the cell before the WT (Fig S4A-C). Giving an initial advantage to the WT allows for the DI infect the cell sooner to maximize its production. On the opposite, as DI MOI gets larger than WT MOI, the shift is towards delays where WT infects the cell before the DI. Giving the DI more advantage than it already has by being faster at replicating and encapsidating can be compensated by an earlier infection of the WT in order to maximize DI production.

4 Discussion

We used a combination of mathematical modeling and empirical measurements to get a better understanding of the mechanisms of interaction between a cooperator, the WT, producing capsid proteins as public goods, and a cheater, the DI, exploiting those capsid proteins from the WT when co-infecting a cell. This type of direct competition affecting the growth of a competitor is known as interference competition. Interestingly, in co-infected cells, we could evidence that WT and DI also compete for shared resources necessary for replication, a phenomenon known as exploitation competition [1–3]. Hence we could identify two types of competition occurring during the co-infection of a cell by WT and DI.

Huang & Baltimore [42] argue that defective particles may influence the development and course of certain viral diseases. DI RNAs are produced through abnormal replication events and during high-multiplicity passage of the original virus [43]. Internal sequences of the original vRNA of DI RNA segments are deleted, whereas holding certain 5' and 3' end-specific sequences of the progenitor vRNA. A recent study on naturally occurring immunostimulatory defective viral genomes (iDVGs) reveals that they are generated during respiratory syncytial virus (RSV) replication and are strong inducers of the innate/natural antiviral immune response to RSV in mice and humans [25].

4.1 Mechanism of defective interference

The precise mechanism of defective interference in poliovirus has been largely unclear, although there have been several classical studies evaluating DI particles [16, 18]. We specifically examined the competition between WT and DI genomes during RNA replication and the consequences of DI capsid exploitation for WT virus production (Figs 1 & 4).

Our model predicts and our experiments provides evidence for three main conclusions. First, the number of WT or DI genomes, taken individually, is lower in dually infected cells compared to singly infected cells (Fig 1C*i*& *ii*), indicating that they compete for a limiting resource for replication. Second, in dually infected cells, DI genomes replicate faster than WT genomes (Fig 1C*iii*), showing the advantage of their shorter genome size [27, 28]. Furthermore, we isolated DI variants with distinct replication fitness, which were used to confirm the model prediction indicating that the WT/DI replication fitness ratio is a major determinant of the outcome of infection. Third, the decrease in WT encapsidated genomes from singly to dually infected cells is two folds larger than that of WT naked genomes (Fig 1D*i*& C*i*), indicating that DI genomes, by trans-encapsidating in capsid proteins produced by the WT, further inhibit WT virions production.

We have designed a minimal mathematical model able to capture key features of the DI/WT interaction during a single-cell replication cycle. We accounted explicitly for depletion of cellular resources and available capsid proteins, the latter solely produced by the WT virus. This has allowed us to accurately describe the reference *in vitro* experimental data, and to predict new data on which the model had not been trained (Fig S2). In particular, the data fitting procedure has provided us with the possibility of estimating model parameters within biologically realistic ranges.

We expected the DI genome to replicate faster than the WT by a factor of approximately the ratio of WT to DI genome lengths, that is 7515bp/5733bp = 1.311. However, the best optimized value of the corresponding parameter P was lower (1.075, Table 1). This discrepancy is most probably due to the time for various processes linked to replication to take place. For example, poliovirus replication first relies on the recruitement of membranes from intracellular organelles (endoplasmic reticulum, Golgi and lysosome) into clusters of vesicles, forming replication organelles [35]. Then, replication starts by the synthesis of a negative strand of RNA, which serves as a template for positive-strand

synthesis [36]. The time for each of these preliminary steps to occur might lower the average difference in replication speed between the WT and DI genomes over the course of infection of a cell. Additionally, the maximum number of replicases per RNA strand might be lower for the DI genome as it is shorter, lowering its overall replication speed compared to the WT [31].

Experimental data suggest that some limiting resources are required and depleted during replication of viral genomes. Those resources might be phospholipids or lipids recruited by the viral machinery for the formation of replication complexes [33, 34] or host proteins involved in viral replication [31]. When both WT and DI co-infect a cell, they are in competition for the exploitation of those shared and limiting resources. As DI replicates faster, it depletes resources faster than WT, affecting WT replication compared to WT-only infections [3]. Additionally, [31] argued that virus genome replication represents a heavy burden for the cell, leading to its pathology and eventual death, and consequently to a slowdown in replication as the virus depletes resources. From fitting the models to the experimental data, we could estimate an initial replication rate of $3.02 - 3.07 \cdot 10^{-2} \text{min}^{-1}$, that can be assimilated to a case where the resources are not limiting. Then, as resources are depleted, the replication rate is predicted to decrease towards 0 logistically (Fig S1F).

4.2 Insights on model fit to experimental data

The reduced model with the logistic equation underestimates the number of viral genome copies in singly infected cells. The logistic equation constrains the time-dependent genomic replication to be the same in both dually and singly infected cells. In other words, this reduced model assumes that depletion of resources required for replication is identical in singly or dually-infected cells. Hence viral genomes do not accumulate less when the other entity is co-infecting. As a result, genome copies are well predicted in dually-infected cells but underestimated in singly-infected cells. On the opposite, the full model is able to recapitulate the impact of resource depletion on RNA genome production in both dually and singly infected cells, as a specific variable for resources and mass action terms are added.

The full model overestimates the number of encapsidated WT genomes in singly infected cells. This result suggests that the WT virus encapsidates less efficiently when it is alone than when it is co-infecting a cell with the DI replicon. For the sake of simplic-

ity, our model assumes that the encapsidation rate of WT is the same in singly- and dually-infected cells (κ), yielding the pointed-out overestimation. One hypothesis for this observation is that products of the DI could benefit to the WT when both co-infect a cell, enhancing WT encapsidation. Indeed, during co-infection, two viruses can exploit a common pool of resources equally [44]. Our model predicts that the DI genomes encapsidate more efficiently than the WT, by a factor ω (= 2.185), hence the factors enhancing DI encapsidation might also help WT encapsidation. In particular, the WT and DI genomes encode non-structural proteases (3C/3CD) which cleave P1 capsid protein precursor into several parts [45, 46]. Upon co-infection, additional expression of proteases by the DI may enhance WT capsid formation, benefiting to the encapsidation of both WT and DI. An additional hypothesis comes from the observation that replication and packaging of poliovirus are functionally coupled [47]. Hence the faster replication of DI might enhance encapsidation of the WT and trans-encapsidation of the DI.

A surprising observation is that the number of encapsidated genomes tend to decrease on average from 7 to 9 hours post transfection (from 410 to 385 for WT in singly infected cells, from 115 to 81 for WT in dually infected cells, and from 355 to 336 for DI in dually infected cells). This decrease is not recapitulated by the model as it does not include a decay term for encapsidated genomes. As the experiment was conducted at the cell population level and then the measurements were divided by the number of successfully transfected cells, it is possible that some cells got lysed before 9 hours post transfection, bringing an artificial decrease in virion production. This decay might also be real, but we chose not to include it in our model because of the too large number of parameters it has.

The cross-validation experiment showed an overall good predictive power of the model, although it underestimated the relative WT output when the DI was transfected in lower quantities than the WT virus (DI-to-WT input ratio of 0.46, Fig S2). Full model simulations with best parameter values overestimates the number of WT encapsidated genomes in singly infected cells while the estimation is accurate in dually infected cells (Fig 3C & D). By normalizing the WT output by its value for WT only infection in the cross-validation experiment, we force the fit on the WT single infection condition, resulting in underestimations of WT relative output in dual infection condition. This can explain the observed discrepancy. It should be emphasized that, even with differing measurements between experiments and simulations (see Material and Methods), the model is able to

recapitulate WT outputs for various inputs, which reinforces its robustness and predictive ability.

4.3 Identification of parameters affecting WT virion production

A sensitivity analysis showed that the most important parameters for the proportion of WT virions at cell lysis when a cell is co-infected by the WT and the DI are DI relative replication factor (P) and encapsidation rate (ω) (Fig 4A-B). These are the only two parameters solely related to the DI construct. Modifications to the DI genome enhancing its replication and/or encapsidation could lead to a decrease in the proportion of WT virions at cell lysis from 23% to 2%. This result highlights the crucial role of exploitation competition [1–3] for resources necessary for genome replication and of interference competition [5] for capsid proteins produced by the WT on the final proportion of WT virions at cell lysis.

4.4 Impact of initial conditions

Overall, our model predicts a crucial impact of temporal spacing and order of infection, as well as initial MOIs, on the proportion of WT virions at cell lysis (Figs 6 and Fig S4). At equal MOIs, the DI particle needs to infect a cell within approximately a 2 hours window before or after the WT in order to produce DI virions, and up to approximately 30 minutes after the WT in order to outcompete the WT in terms of burst sizes (Fig 6A). When simulaneously co-infecting a cell, the DI particles will maximize their virion production when WT and DI initial MOIs are approximately equivalent, and the WT particles will maximize their virion production when WT MOI is larger than DI MOI (Fig 6B-C). At equal MOIs, the difference between DI and WT virion production is maximized at approximately simultaneous co-infection of a cell. When WT MOI is larger than DI MOI, this difference maximization is obtained when the DI infects the cell before the WT. Conversely, when DI MOI is larger than WT MOI, it is obtained when the WT infects the cell before the DI (Fig S4).

These results are in agreement with those of [48], who found that the extent of interference, assessed by the yield of WT poliovirus, is inversely proportional to the percentage of DI in the inoculum, and that it is also affected by varying the time interval between primary and secondary infection of a cell. In their viewpoint article, [2] highlight the importance

of initial conditions, such as relative initial frequencies, temporal spacing and order of inoculation on the evolution of a population. An earlier review [49] also emphasized this aspect, while focusing on the exclusion of one virus strain by another. Experimental studies have shown inhibition of superinfection by a resident strain, in bacteria [50] and in viruses [51]. Another experiment on bacteria showed that the inhibition of superinfection was dose-dependent and also depended on the order of inoculation [52]. It is also known that picornaviruses rapidly induce resistance of the host cell to superinfection by the same virus, most probably because of inactivation or internalization of poliovirus receptors [53]. Importantly, [47] found that preaccumulated replicon RNAs are not trans-encapsidated by capsids made from a coinfecting helper virus, showing that only newly synthesized poliovirus RNAs are packaged. This could mean that, when the DI is the first to infect a cell, the genomes replicated before WT superinfection would not get trans-encapsidated by WT capsids. Hence our predictions might overestimate the DI burst size when DI is the first to infect a cell. This assumption would need to be tested in future experimental work.

4.5 Limited resource and co-evolution

The competition between WT poliovirus and DI particles within cell can be analysed in light of evolutionary game theory. For a game between WT cooperators and DI defectors, the pay-off matrix features a fitness of zero in the case of a population composed only of DIs, because they are unable to reproduce [54]. With such a feature, the evolution of a mixed WT and DI population is predicted to result in a polymorphic equilibrium, despite the greater pay-off that would result if the population was composed only of WT cooperators [54]. These strategies of cooperation and defection are common in viruses, as co-infection of the same host cell induces competition for shared intracellular products [54]. Evidence of such co-infections exists *in vivo*, as reported in the 2006 outbreak of dengue in India, where nearly 20% of infections comprised multiple dengue serotypes [1, 55]. Long-term transmission of defective dengue viruses was also found in virus populations in humans and Aedes mosquitoes [56]. Defective viruses were suggested to increase the overall incidence of transmission by modifying the virulence-transmissibility trade-off [57]. Resource availability can have important consequences on the dynamics and evolution of mixed pathogen populations [2, 58, 59]. For example, playing on resource availability

could allow to slow the evolution of resistance to antimicrobial drugs [60]. In the case of DI particles, their presence within-cells infected by a WT virus is decreasing the number of resources available to the WT for replication and encapsidation, lowering WT virions production. Hence DI particles could be used to control WT infections, by lowering WT viral load, thereby facilitating further action of the immune system and/or drugs to clear the infection [42].

4.6 Perspectives

It has been suggested that the potential of DI particles to compete against a WT virus can be exploited to develop a new type of therapeutic antiviral strategy based on defective interfering particle competition [61]. Our model and the sensitivity analysis we have performed suggest that parameters P, the DI-to-WT replication ratio, and ω, the DI-to-WT encapsidation ratio, are the first and second most important parameters impacting the proportion of WT virions at cell lysis. Therefore, a rational strategy to strengthen interference activity of DI genomes and thus reduce the production of WT virions is to modify DI genomes towards higher replication speed and encapsidation efficiency. Such improvements may be realized by taking advantage of the evolvability of DI genomes. Serial co-passages of WT and DI particles followed by genetic analyses, as done in Fig. 5A, B and C, would allow for the screening of other mutations providing higher replication or encapsidation of the DI. Also, the production of shorter DI genomes could lead to its faster replication.

Improving the interference at the intracellular level may cause less inhibition of WT viral load at the intercellular level, as there could be trade-offs. A reduced production of WT particles within-cells could result in a decreased MOI of WT viruses for the next infection cycle, and also to a decreased probability of a cell being co-infected. Furthermore, the narrow window of delay of co-infection for the DI to outcompete the WT as shown in Fig 6A also suggests the importance of simultaneous infection. Interestingly, recent studies show several possibilities for how co-infection is or can be favored [62–64]. Notably, the existence of vesicles containing multiple copies of virions as well as bacteria binding virions may increase the probability of simultaneous co-infection [62, 63]. Erickson et al. [64] reported that poliovirus binds lipopolysaccharide of bacteria, allowing co-infection of mammalian cells even at a low MOI. Finally, the potential of the combined DI-WT

system to synergistically trigger an effective innate immune response (e.g. interferon) is also a potential avenue of investigation for the rational design of an antiviral therapy.

While ecological studies for the control of pathogen populations mainly focus on preventing or slowing down the emergence of drug resistance [60, 65, 66] or on the evolution of virulence [67, 68], we take an original approach here by rather studying how to use cheater defective pathogens, competing more efficiently for shared resources, for the control of disease-inducing pathogens. Since we learned the mechanisms of intracellular interference, in a future work we would like to apply these findings for the study of the competition between WT and DI at the larger level of the tissue, embedding intracellular knowledge. It would allow us to draw guidelines to optimize DI particles at this level, based on WT viral load inhibition, and further confirm their efficiency *in vivo*.

5 Material and Methods

5.1 Competition experiment between defective genomes and wild-type genomes

5.1.1 Cells

HeLaS3 cells (ATCC CCL-2.2) provided by R. Geller and J. Frydman (Stanford University) were maintained in 50% Dulbecco's modified Eagle medium and 50% F-12 medium (DMEM/F12) supplemented with 10% newborn calf serum (NCS), 100 U/ml penicillin, 100 U/ml streptomycin and 2 mM glutamine (Invitrogen).

5.1.2 Construction of viral cDNA plasmids

The cDNA plasmid prib(+)XpA, encoding the genome of poliovirus type 1 Mahoney strain under T7-promoter and hammerhead ribozyme sequences, was reported previously [69]. Plasmid prib(+)XpA was digested by *NruI* and *SnaBI* (New England Biolabs) and ligated to produce prib(+)XpA lacking the poliovirus capsid-encoding region from 1175 to 2956 (prib(+)XpA-Δ1175-2956).

5.1.3 *In vitro* RNA transcription

Plasmids prib(+)XpA and prib(+)XpA-Δ1175-2956 were digested by *EcoRI* or *PvuII*. Linearized plasmids were used as templates to obtain WT and DI genomic RNAs by *in vitro* transcription using RiboMAX^{TM} Large Scale RNA Production Systems (Promega). *In vitro* transcribed RNAs were purified by phenol-chloroform extraction and the quality of purified RNAs was analyzed by electrophoresis on a 1% agarose gel in tris-acetate-EDTA Buffer (TAE) .

5.1.4 Transfection of defective interfering and wild-type genomes

Monolayer of HeLaS3 cells was trypsinized and washed three times in D-PBS. Cells were resuspended in 1 ml D-PBS and the number of cells were counted on a hemacytometer, followed by adjusting the concentration to 1×10^7 cells/ml. 800 μl of cells and virus RNAs (5μg of WT genomes and/or different amounts of DI genomes described later) were combined in a chilled 4-mm electroporation cuvette and incubated 20 minutes on ice. Cells were electroporated (voltage = 250 V, capacitance = 1000 μF) using Gene Pulser II (Bio-Rad), washed two times, and recovered in 14 ml prewarmed (37 °C) DMEM/F12 medium with 10% NCS. Samples were distributed on 24 well plates (250 μl/well). Samples were collected at different time points (0, 3, 6, 9 hours for titration, and 0, 2, 3.5, 5, 7, 9 hours for RNA extraction) after electroporation. For titration and evaluation of encapsidated RNAs, samples were then frozen and thawed three times, followed by centrifugation at 2,500 g for 5 minutes, and supernatants were collected. Samples for evaluation of encapsidated RNAs were further treated with mixture of RNase A (20 μg/ml) and RNase T1 (50 U/ml) (Thermo Fisher Scientific) for three hours. Samples were stored at −80 °C.

5.1.5 Titration of virus samples

Monolayers of HeLaS3 cells in 6-well plates were infected with 250 μl of serially diluted virus samples at 37 °C for 1 hour and then overlaid with DMEM/F12 including 1% agarose. After 48 hours of infection, infected cells were fixed by 2% formaldehyde and stained by crystal violet solution. Titers were calculated by counting the number of plaques and multiplying their dilution rates.

5.1.6 RNA extraction

250 μl of samples was added to 750 μl of TRI-reagent LS (Sigma Aldrich), and RNAs were extracted following the kit protocol. Briefly, 200 μl of chloroform was added to each sample, shaken vigorously, and incubated at room temperature for 10 minutes. Then samples were centrifuged at 12,000 g for 15 minutes at 4 °C. The upper aqueous phase was transferred to a fresh tube and 0.5 ml of isopropanol was added. After incubation at room temperature for 10 minutes, samples were centrifuged at 12,000 g for 8 minutes at 4 °C to precipitate RNAs at the bottom of the tube. The supernatant was removed and the residue was washed by 1 ml of 75% ethanol. After centrifugation at 7,500 g for 5 minutes at 4 °C, the RNA pellets were dried for 5-10 minutes. RNAs were resuspended in nuclease-free water.

5.1.7 Reverse transcription

2.5 μl of RNA samples was mixed with 0.5 μl of 2 μM primer (5'-CTGGTCCTTCAGTGGTACTTTG-3'), 0.5 μl of 10 mM dNTP mix, and 2.5 μl of nuclease-free water. Samples were incubated at 65 °C for 5 minutes, and then placed on ice for 1 minute. After adding 10 μl of cDNA synthesis mix (1 μl of 10× RT buffer, 2 μl of 25 mM MgCl2, 1 μl of 0.1 M DTT, 1 μl of RNaseOUT and 1 μl of Superscript III RT enzyme), samples were incubated at 50 °C for 50 minutes, and then at 85 °C for 5 minutes to terminate reactions. 1 U of RNase H was added to each sample, followed by incubation for 20 minutes at 37 °C. Then, 0.1 U of Exonuclease I was added to each sample, followed by incubation at 37 °C for 30 minutes and at 80 °C for 15 minutes to terminate reactions. cDNA samples were stored at −20 °C.

5.1.8 Design of primers and Taqman probes

Primers and Taqman probes for droplet digital PCR assay were designed with PrimerQuest Tool (Integrated DNA Technologies). The primers and probe for WT genomes are 5'-CCACATACAGACGATCCCATAC-3', 5'-CTGCCCAGTGTGTGTAGTAAT-3', and 5'-6-FAM-TCTGCCTGTCACTCTCTCCAGCTT-3'-BHQ1. The primers and probe for DI genomes are 5'-GACAGCGAAGCCAATCCA-3', 5'-CCATGTGTAGTCGTCCCATTT-3', and 5'-HEX-ACGAAAGAG/ZEN/TCGGTACCACCAGGC-3'-IABkFQ.

5.1.9 Droplet digital PCR assay

2 μl of serially diluted cDNA samples was mixed with 10 μl of 2× ddPCR supermix for probes (Bio-Rad), 1 μl of 20× WT primers/probe, 1 μl of 20× DI primers/probe, and 6 μl of nuclease-free water. 20 μl reaction mix of each sample was dispensed into the droplet generator cartridge, followed by droplet production with QX100 droplet generator (Bio-Rad). Then PCR was performed on a thermal cycler using the following parameters: 1 cycle of 10 minutes at 95 °C, 30 cycles of 30 sec at 94 °C and 1 minute at 60 °C, 1 cycle of 10 minutes at 98 °C, and held at 12 °C. Positive and negative droplets were detected by QX100 droplet reader (Bio-Rad). The data was analyzed with the QuantaSoft™ Software (Bio-Rad).

5.2 Model reduction

As our mathematical model (Eqs 1 - 4) presents a classical problem of parameter identifiability, we built a lower dimensional model to solve this problem by assuming that the decrease in resources due to viral uptake for replication follows a logistic decreasing function. This assumption was verified by analyzing the curves of $R(t)\theta\varepsilon$ as a function of time on a first set of "blind" optimizations (data not shown). Thus, we can recast the model using the following lower dimensional description:

$$\frac{dG_{WT}}{dt} = \Lambda(t)G_{WT} - c_g\kappa C G_{WT} - \alpha G_{WT} \quad (7)$$

$$\frac{dC}{dt} = \eta\Lambda(t)G_{WT} - \kappa(G_{WT} + \omega G_{DI})C - \beta C \quad (8)$$

$$\frac{dG_{DI}}{dt} = P\Lambda(t)G_{DI} - \omega c_g\kappa C G_{DI} - \alpha G_{DI} \quad (9)$$

$$\Lambda(t) = \frac{L}{1 + e^{-s(t-t_0)}} \quad (10)$$

The logistic function (Eq 10) is characterized by the curve's maximum value L and steepness s, and the time of the sigmoid's midpoint t_0. While this reduced version only decreases the number of parameters to be estimated by one (L, s and t_0 instead of θ, ε, λ and γ), it partially solves the identifiability problem by removing biologically interpretable parameters and just assuming a logistic function for resource uptake and replication.

5.3 Fit to experimental data

The model was fitted to the experimental data in order to estimate model parameters describing our biological system. Preliminary experimental data on the evolution of genome copy number showed that replication starts around 2 hours post transfection (data not shown). Indeed, there are several steps of poliovirus infection cycle before replication can start, including translation of positive-sense genomes [36] and transition from a linear, translating RNA to a circular RNA competent for replication [70–73]. As our model does not account for those first steps, we only used experimental data from 2 hours post transfection for parameter estimation.

Raw experimental data are WT and DI total RNA copy number (g_{WT}^{tot} and g_{DI}^{tot}) and RNAse treated genome copy number (v_{WT} and v_{DI}). The former corresponds to the total number of genomes (naked and encapsidated) and the latter to the number of encapsidated genomes. The numbers of WT and DI naked (i.e. non-encapsdisated) genomes are thus: $g_{WT} = g_{WT}^{tot} - v_{DI}$ and $g_{DI} = g_{DI}^{tot} - v_{DI}$. Additionally, as raw data was obtained at the cell population level, it was normalized by the average number of successfully transfected cells (data not shown) in order to get the average number of naked and encapsidated WT and DI genomes per cell.

In all, experimental data comprises three replicates of independent populations sampled at 2, 3.5, 5, 7 or 9 hours post transfection. Three different conditions were tested: (i) cells dually transfected by WT and DI genomes, (ii) cells transfected by WT genomes only and (iii) cells transfected by DI genomes only. Transfected volumes of WT and DI genomes were calibrated to a ratio of WT:DI = 4:1 in order to approximately obtain a ratio of 1:1 after transfection (preliminary experiment, data not shown).

Parameter estimation was achieved through nlminb optimization function in R software [74] embedded in an iterative process. Each optimization consisted in minimizing the sum of the least squares between experimental and simulated normalized data points for all variables and conditions. The least square function is as:

$$\begin{aligned} LS \;=\; & \sum_r \sum_t \underbrace{\left[(\bar{G}_{WT}(t) - \bar{g}_{WT}(t,r))^2 + (\bar{G}_{DI}(t) - \bar{g}_{DI}(t,r))^2 + (\bar{C}_{WT}(t) - \bar{v}_{WT}(t,r))^2 + (\bar{C}_{DI}(t) - \bar{v}_{DI}(t,r))^2\right]}_{\text{Dually transfected cell}} \\ & + \sum_r \sum_t \underbrace{\left[(\bar{G}_{WT}(t) - \bar{g}_{WT}(t,r))^2 + (\bar{C}_{WT}(t) - \bar{v}_{WT}(t,r))^2\right]}_{\text{WT genome transfected cell}} + \sum_r \sum_t \underbrace{\left[(\bar{G}_{DI}(t,r) - \bar{g}_{DI}(t,r))^2\right]}_{\text{DI genome transfected cell}} \end{aligned} \tag{11}$$

with r indicating the replicate number and t the sampling time ($t = 3.5$ to 9 hours post transfection). Initial conditions for all variables in all infection conditions were obtained from averaging experimental observations over the 3 replicates at $t_0 = 2$ hours post transfection. In Eq. (11), we define:

$$\bar{x_i} = \frac{\log(x_i + 1)}{\max(g_i)} \, , \, \bar{y_i} = \frac{\log(y_i + 1)}{\max(v_i)}$$

with x, resp. y, being either experimental (g, resp. v) or numerical (G, resp. C) naked, resp. encapsidated, genomes data and i for WT or DI.

The iterative process was applied as follows (see also Fig S3 for a schematic representation). Boundaries on parameter values were defined based on a first set of "blind" optimizations, the intervals still remaining large and realistic. For each parameter p, let us denote p_{min} the lower boundary and p_{max} the upper boundary. For the first iteration, random values of parameters were drawn from uniform distributions, as $p_{start} \sim \text{Unif}(p_{min}, p_{max})$, defining the starting point for optimization. Let us denote $\widetilde{p}$ the optimized parameter value. In subsequent iterations, the starting point for each parameter was then randomly drawn from a uniform distribution, as $p_{start} \sim \text{Unif}\left(\max(0.95 \cdot \widetilde{p}, p_{min}), \min(1.05 \cdot \widetilde{p}, p_{max})\right)$. In all, 20 iterations were conducted, and this iterative procedure was implemented 250 times, each time with a different random starting point in the first iteration. Thus, $250 \times 20 = 5000$ optimizations were performed in total.

The goodness of fit was evaluated by ordinary least square (Eq. (11)) and sum of residuals R^2 between experimental and simulated normalized data.

This optimization procedure was applied in two steps. In the first step, the optimization was performed on the reduced version of the model (Eqs 5-10), thus estimating nine parameters: the six parameters corresponding to (i) the DI (P and ω), (ii) the production of capsids (η), (iii) the encapsidation process (κ) and (iv) the decay rates of genomes and capsids (α and β); and the three parameters of the logistic function representative of the time-dependent replication rate (L, s and t_0). In the second step, the six redundant parameters between the reduced and full version of the model (P, ω, η, κ, α and β) were fixed to their best estimated value obtained during the first step. The remaining four parameters (θ, ϵ, λ and γ) were estimated by optimizing the full version of the model (Eqs 1-6).

5.4 Model predictions

5.4.1 Cross-validation

We cross validate the results of our optimization procedure by assessing how well the model is able to predict the relative WT virus burst size for various WT to DI initial ratios (after transfection) for which it has not been trained. We first obtain an optimal set of model parameters on our time series experimental data (g and v) featuring initial WT:DI = 1:1. We then test five additional DI-to-WT initial ratios, ranging from 0 to 3.6. Initial conditions for model simulations were set as the average of experimental values for each of the five initial ratios.

In the cross-validation experiment, evaluation of the relative WT virus burst size was based on the count of plaque-forming units (PFUs). In the time-series experiment that was used for parameter estimation, the number of WT virions (v_{WT}) was estimated by digital droplet PCR. Assuming that the ratio of WT infectious to non-infectious particles and the multiplicity of infection (MOI) of WT virus are both constant independently of initial conditions, the relative PFU of WT virus for each initial condition should be a good proxy of the relative WT burst size.

The experiment was conducted on a cell population, and then the measurements were normalized by the number of successfully transfected cells. In some cases, the average experimental MOIs were small, potentially leading to not all cells being co-infected by WT and DI genomes. We integrated this aspect in our simulated burst size calculations, with the probabilities that a cell would be infected by both DI and WT genomes or only by WT genomes. We assume that the number of DI genomes infecting a cell X_{DI} results from a Poisson distribution of parameter the average DI MOI n_{DI}, as $X_{DI} \sim Pois(n_{DI})$. The probability that no DI genome enters a cell is thus $P(X_{DI} = 0) = e^{-n_{DI}}$. Conversely, the probability that at least one DI genome enters a cell is $1 - e^{-n_{DI}}$. The expressions are equivalent for the WT virus. Let us denote the WT burst size in WT-DI infection as $\mathcal{B}_{WT}(WT-DI)$ and the WT burst size in WT-only infection as $\mathcal{B}_{WT}(WT)$. We weighted WT simulated burst sizes as follows: $\mathcal{B}_{WT} = (1 - e^{-n_{DI}})(1 - e^{-n_{WT}})\mathcal{B}_{WT}(WT - DI) + e^{-n_{DI}}(1 - e^{-n_{WT}})\mathcal{B}_{WT}(WT)$.

WT PFU experimental values and WT burst size model predictions ($\mathcal{B}_{WT}$) were normalized for all initial ratios by their respective values in the absence of DI genome (i.e. DI-to-WT initial ratio of 0). For the experimental data the average over the three repli-

cates was taken for normalization. The performance of the model to predict relative WT burst size was evaluated by R^2 and p-value of a Pearson correlation test between experimental and simulated datapoints.

5.4.2 Sensitivity analysis

A sensitivity analysis was performed to assess the relative importance of each parameter on the proportion of WT virions at cell lysis, defined as:

$$\Phi_{WT} = \frac{\mathcal{B}_{WT}}{\mathcal{B}_{WT} + \mathcal{B}_{DI}} \tag{12}$$

Based on parameter estimation, each parameter was approximately varied by $\pm 50\%$ of its best estimated value. Based on these boundaries, each parameter was allocated a vector of five equidistant values (except for α that was not varied because it was estimated at 0, see Tab 1). Then, all distinct combinations of parameter values were tested according to a full factorial design. In all, $5^9 = 1,953,125$ simulations of the full model were performed. All simulations started at time 0 hours post transfection with 10 copies of WT and DI genomes ($G_{WT}(0) = G_{DI}(0) = 10$), no capsids nor encapsidated genomes ($C(0) = C_{WT}(0) = C_{DI}(0) = 0$), and $R(0) = \lambda/\gamma$. Simulations were conducted until 9 hours post transfection. An analysis of variance (ANOVA function in R software) was then conducted to assess the importance of each parameter and their second-order interactions on the variance of Φ_{WT}.

5.4.3 Impact of delay and multiplicities of infection on WT and DI burst sizes

In the experiment, WT and DI genomes were co-transfected to cells and in quantities yielding an MOI ratio of approximately WT:DI = 1:1. We conducted two sets of simulations to study the impact of varying either (i) the time between cell infection by WT and DI or (ii) the MOIs of WT and DI on their burst sizes. All the simulations were conducted on the full version of the model (Eqs 1-6). In the first set of simulations, WT and DI burst sizes were recorded for various delays between primary and secondary infection of a cell, ranging from -7 to +7 hours for the time of DI infection compared to the WT. The MOI upon infection of the cell was set to 10 for both WT and DI (i.e. $G_{WT}(0) = 10$ and $G_{DI}(t_d) = 10$, with t_d the delay for DI infection), the number of capsids and encapsidated

genomes to 0 and $R(0)$ to λ/γ. In the second set of simulations, WT and DI burst sizes were recorded for various WT and DI initial MOIs, ranging from 0 to 1000. All the other variables were set as described for the study of delays. Then, WT burst sizes were normalized by the WT burst size corresponding to WT:DI = 1:0 initial MOIs (i.e. infection by the WT virus only at low MOI), and DI burst sizes by the DI burst size corresponding to WT:DI = 1:1 initial MOIs (i.e. infection by both WT and DIs at low MOI).

6 Acknowledgments

This work is supported by the Defense Advanced Research Projects Agency (DARPA) program INTERCEPT (contract No. HR0011-17-2-0027).

7 Author contributions

Conception of experiments: YS, RA; Conducting experiments: YS, WS, YX; Experimental data analysis: YS, ER, JV, WS, YX, AC, ZW; Model conception: JV, ER, IR, SB; Model simulations: JV, ER; Visualization: YS, ER, JV, RA; Writing original draft: YS, ER; Review and editing: YS, ER, JV, IR, SB, RA; Supervision: IR, SB, RA; Funding acquisition: IR, SB, RA.

References

1. Mideo, N. Parasite adaptations to within-host competition. *Trends in Parasitology* **25,** 261–268 (2009).

2. Read, A. F. & Taylor, L. H. The ecology of genetically diverse infections. *Science* **292,** 1099–1102 (2001).

3. Bashey, F. Within-host competitive interactions as a mechanism for the maintenance of parasite diversity. *Phil. Trans. R. Soc. B* **370,** 20140301 (2015).

4. Holt, R. D. Predation, apparent competition, and the structure of prey communities. *Theoretical Population Biology* **12,** 197–229 (1977).

5. Schoener, T. W. Field experiments on interspecific competition. *The American Naturalist* **122,** 240–285 (1983).

6. Racaniello, V. R. in *Fields Virology* (eds David, K. M. & Peter, H. M.) 6th, 23753–26073 (Lippincott Williams & Wilkins, Philadelphia, 2013). ISBN: 9781451105636. doi:9781451105636.

7. Holland, J. *et al.* Rapid Evolution of RNA Genomes. *Science* **215,** 1577–1585 (1982).

8. Drake, J. W. Rates of spontaneous mutation among RNA viruses. *Proc. Natl. Acad. Sci. USA* **90,** 4171–4175 (1993).

9. Nowak, M. A. What is a Quasispecies? *Trends in Ecology & Evolution* **7,** 118–121 (1992).

10. Eigen, M. Viral quasispecies. *Scientific American* **269,** 42–49 (1993).

11. Biebricher, C. K. & Eigen, M. in (ed (Eds), D. E.) 1–31 (Springer, Berlin, Heidelberg, 2006). doi:10.1007/3-540-26397-7_1.

12. Von Magnus, P. Incomplete forms of influenza virus. *Advances in virus research* **2,** 59–79 (1954).

13. Hirst, G. K. Genetic recombination with Newcastle disease virus, polioviruses, and influenza. *Cold Spring Harb. Symp. Quant. Biol.* **27,** 303–309 (1962).

14. Sergiescu, D., Horodniceanu, F., Klein, R. & Crainic, R. Genetic transfer of guanidine resistance from type 2 to type 1 poliovirus. *Archiv für die gesamte Virusforschung* **18,** 231–243 (1966).

15. Kuge, S., Saito, I. & Nomoto, A. Primary structure of poliovirus defective-interfering particle genomes and possible generation mechanisms of the particles. *Journal of molecular biology* **192,** 473–87. ISSN: 0022-2836 (1986).

16. Lundquist, R. E., Sullivan, M. & Maizel, J. V. Characterization of a new isolate of poliovirus defective interfering particles. *Cell* **18,** 759–69. ISSN: 0092-8674 (1979).

17. Bellett, A. J. D. & Cooper, P. D. Some Properties of the Transmissible Interfering Component of Vesicular Stomatitis Virus Preparations. *Microbiology* **21,** 498–509. ISSN: 1350-0872 (1959).

18. Cole, C. N., Smoler, D., Wimmer, E. & Baltimore, D. Defective interfering particles of poliovirus. I. Isolation and physical properties. *Journal of virology* **7,** 478–85. ISSN: 0022-538X (1971).

19. Calain, P., Monroe, M. C. & Nichol, S. T. Ebola virus defective interfering particles and persistent infection. *Virology* **262,** 114–128. ISSN: 0042-6822 (1999).

20. Li, D. *et al.* Defective interfering viral particles in acute dengue infections. *PLoS ONE* **6,** e19447 (2011).

21. Saira, K. *et al.* Sequence Analysis of In Vivo Defective Interfering-Like RNA of Influenza A H1N1 Pandemic Virus. *Journal of Virology* **87,** 8064–8074. ISSN: 0022-538X (2013).

22. Huang, A. S. Defective Interfering Viruses. *Annual Review of Microbiology* **27,** 101–118. ISSN: 0066-4227 (1973).

23. Vasilijevic, J. *et al.* Reduced accumulation of defective viral genomes contributes to severe outcome in influenza virus infected patients. *PLoS Pathog* **13,** e1006650 (2017).

24. Dimmock, N. J. & Easton, A. J. Cloned defective interfering Influenza RNA and a possible pan-specific treatment of respiratory virus diseases. *Viruses* **7,** 3768–3788 (2015).

25. Sun, Y. *et al.* Immunostimulatory defective viral genomes from respiratory syncytial virus promote a strong innate antiviral response during infection in mice and humans. *PLoS pathogens* **11,** e1005122 (2015).

26. Kaplan, G. & Racaniello, V. R. Construction and characterization of poliovirus subgenomic replicons. *Journal of virology* **62,** 1687–96. ISSN: 0022-538X (1988).

27. Holland, J. in (eds Fields, B. & Knipe, D.) 2nd ed., 151–165 (Raven Press, New York, 1991).

28. Chao, L. & Elena, S. F. Nonlinear trade-offs allow the cooperation game to evolve from Prisoner's Dilemma to Snowdrift. *Proc. R. Soc. B* **284,** 20170228 (2017).

29. Rouzine, I. M. & Weinberger, L. S. Design requirements for interfering particles to maintain coadaptive stability with HIV-1. *Journal of virology* **87,** 2081–93. ISSN: 1098-5514 (2013).

30. Baltimore, D., Girard, M. & Darnell, J. E. Aspects of the synthesis of poliovirus RNA and the formation of virus particles. *Virology* **29,** 179–189 (1966).

869 31. Regoes, R. R., Crotty, S., Antia, R. & Tanaka, M. M. Optimal Replication of Po-
870 liovirus within Cells. *The American Naturalist* **165,** 364–373 (2005).

871 32. Guinea, R. & Carrasco, L. Phospholipid biosynthesis and poliovirus genome replica-
872 tion, two coupled phenomena. *The EMBO Journal* **9,** 2011–2016 (1990).

873 33. Nchoutmboube, J. A. *et al.* Increased Long Chain acyl-Coa Synthetase Activity and
874 Fatty Acid Import Is Linked to Membrane Synthesis for Development of Picornavirus
875 Replication Organelles. *PLoS Pathog* **9,** e1003401 (2013).

876 34. Altan-Bonnet, N. Lipid tales of viral replication and transmission. *Trends in Cell*
877 *Biology* **27,** 201–213 (2017).

878 35. Den Boon, J. A. & Ahlquist, P. Organelle-like membrane compartmentalization of
879 positive-strand RNA virus replication factories. *Annual review of microbiology* **64,**
880 241–256 (2010).

881 36. Novak, J. E. & Kirkegaard, K. Coupling between genome translation and replication
882 in an RNA virus. *Genes & Dev* **8,** 1726–1737 (1994).

883 37. Semler, B. L. & Wimmer, E. *Molecular biology of picornaviruses* (ASM press Wash-
884 ington, DC, Washington, D.C., 2002).

885 38. Burrill, C. P., Strings, V. R. & Andino, R. Poliovirus: generation, quantification,
886 propagation, purification, and storage. *Current protocols in microbiology* **29,** 15H.1.1–
887 15H.1.27 (2013).

888 39. Bird, S. W., Maynard, N. D., Covert, M. W. & Kirkegaard, K. Nonlytic viral spread
889 enhanced by autophagy components. *Proceedings of the National Academy of Sci-*
890 *ences* **111,** 13081–13086 (2014).

891 40. Acevedo, A. & Andino, R. Library preparation for highly accurate population se-
892 quencing of RNA viruses. *Nature Protocols* **9,** 1760–1769 (2014).

893 41. Acevedo, A., Brodsky, L. & Andino, R. Mutational and fitness landscapes of an RNA
894 virus revealed through population sequencing. *Nature* **505,** 686–690 (2014).

895 42. Huang, A. S. & Baltimore, D. Defective viral particles and viral disease processes.
896 *Nature* **226,** 325–327. ISSN: 0028-0836 (1970).

897 43. Perrault, J. in *Initiation Signals in Viral Gene Expression* 151–207 (Springer, 1981).

898 44. Novella, I. S., Reissig, D. D. & Wilke, C. O. Density-Dependent Selection in Vesicular
899 Stomatitis Virus. *Journal of Virology* **78,** 5799–5804 (2004).

900 45. Burns, C. C., Lawson, M. A., Semler, B. L. & Ehrenfeld, E. Effects of mutations in
901 poliovirus 3Dpol on RNA polymerase activity and on polyprotein cleavage. *Journal*
902 *of virology* **63,** 4866–4874 (1989).

903 46. Ypma-Wong, M. F., Dewalt, P. G., Johnson, V. H., Lamb, J. G. & Semler, B. L.
904 Protein 3CD is the major poliovirus proteinase responsible for cleavage of the P1
905 capsid precursor. *Virology* **166,** 265–270 (1988).

906 47. Nugent, C. I., Johnson, K. L., Sarnow, P. & Kirkegaard, K. Functional coupling
907 between replication and packaging of poliovirus replicon RNA. *Journal of virology*
908 **73,** 427–435 (1999).

909 48. Cole, C. N. & Baltimore, D. Defective interfering particles of poliovirus: III. Inter-
910 ference and enrichment. *Journal of molecular biology* **76,** 345–361 (1973).

911 49. Henle, W. Interference phenomena between animal viruses: a review. *The Journal*
912 *of Immunology* **64,** 203–236 (1950).

913 50. Berchieri, A. & Barrow, P. Further studies on the inhibition of colonization of the
914 chicken alimentary tract with Salmonella typhimurium by pre–colonization with an
915 avirulent mutant. *Epidemiology & Infection* **104,** 427–441 (1990).

916 51. Hart, A. R. & Cloyd, M. W. Interference patterns of human immunodeficiency viruses
917 HIV-1 and HIV-2. *Virology* **177,** 1–10 (1990).

918 52. Lipsitch, M. *et al.* Competition among Streptococcus pneumoniae for intranasal
919 colonization in a mouse model. *Vaccine* **18,** 2895–2901 (2000).

920 53. Koch, F. & Koch, G. *The molecular biology of poliovirus* (Springer-Verlag/Wien,
921 New York, 1985).

922 54. Turner, P. E. & Chao, L. Prisoner's dilemma in an RNA virus. *Nature* **398,** 441–443
923 (1999).

924 55. Bharaj, P. *et al.* Concurrent infections by all four dengue virus serotypes during an
925 outbreak of dengue in 2006 in Delhi, India. *Virology Journal* **5,** 1–5 (2008).

926 56. Aaskov, J., Buzacott, K., Thu, H. M., Lowry, K. & Holmes, E. C. Long-term trans-
927 mission of defective RNA viruses in humans and Aedes mosquitoes. *Science* **311,**
928 236–238 (2006).

929 57. Ke, R., Aaskov, J., Holmes, E. C. & Lloyd-Smith, J. O. Phylodynamic analysis of
930 the emergence and epidemiological impact of transmissible defective dengue viruses.
931 *PLoS pathogens* **9,** e1003193 (2013).

932 58. Wale, N., Sim, D. G. & Read, A. F. A nutrient mediates intraspecific competition
933 between rodent malaria parasites *in vivo*. *Proc. R. Soc. B* **284,** 20171067 (2017).

934 59. Turner, P. E. & Chao, L. Sex and the evolution of intrahost competition in RNA
935 virus φ6. *Genetics* **150,** 523–532 (1998).

936 60. Wale, N. *et al.* Resource limitation prevents the emergence of drug resistance by
937 intensifying within-host competition. *PNAS* **114,** 13774–13779 (2017).

938 61. Frensing, T. Defective interfering viruses and their impact on vaccines and viral
939 vectors. *Biotechnology journal* **10,** 681–689 (2015).

940 62. Robinson, C. M., Jesudhasan, P. R. & Pfeiffer, J. K. Bacterial lipopolysaccharide
941 binding enhances virion stability and promotes environmental fitness of an enteric
942 virus. *Cell host & microbe* **15,** 36–46 (2014).

943 63. Chen, Y.-H. *et al.* Posphatidylserine Vesicles Enable Efficient En Bloc Transmission
944 of Enteroviruses. *Cell* **160,** 619–630 (2015).

945 64. Erickson, A. K. *et al.* Bacteria facilitate viral co-infection of mammalian cells and
946 promote genetic recombination. *Cell Host & Microbe* **23,** 5–6 (2018).

947 65. Day, T., Huijben, S. & Read, A. F. Is selection relevant in the evolutionary emergence
948 of drug resistance? *Trends in Microbiology* **23,** 126–133 (2015).

949 66. Roux, D. *et al.* Fitness cost of antibiotic susceptibility during bacterial infection.
950 *Science Translational Medicine* **7,** 297ra114 (2015).

951 67. Frank, S. A. Models of Parasite Virulence. *The Quarterly Review of Biology* **71.**
952 PMID: 8919665, 37–78 (1996).

953 68. Brown, S. P., Inglis, R. F. & Taddei, F. Evolutionary ecology of microbial wars:
954 within-host competition and (incidental) virulence. *Evolutionary Applications* **2,** 32–
955 39 (2009).

956 69. Herold, J. & Andino, R. Poliovirus Requires a Precise 5' End for Efficient Positive-
957 Strand RNA Synthesis. *Journal of Virology* **74,** 6394–6400 (2000).

958 70. Gamarnik, A. V. & Andino, R. Switch from translation to RNA replication in a
959 positive-stranded RNA virus. *Genes & Dev* **12,** 2293–2304 (1998).

960 71. Gamarnik, A. V. & Andino, R. Interactions of Viral Protein 3CD and Poly(rC)
961 Binding Protein with the 5' Untranslated Region of the Poliovirus Genome. *Journal*
962 *of Virology* **74,** 2219–2226 (2000).

963 72. Herold, J. & Andino, R. Poliovirus RNA Replication Requires Genome Circulariza-
964 tion through a Protein-Protein Bridge. *Molecular Cell* **7,** 581–591 (2001).

965 73. Schulte, M. B., Draghi, J. A., Plotkin, J. B. & Andino, R. Experimentally guided
966 models reveal replication principles that shape the mutation distribution of RNA
967 viruses. *eLife* **4,** e03753 (2015).

968 74. Gay, D. M. Usage summary for selected optimization routines. *Computing science*
969 *technical report* **153,** 1–21 (1990).

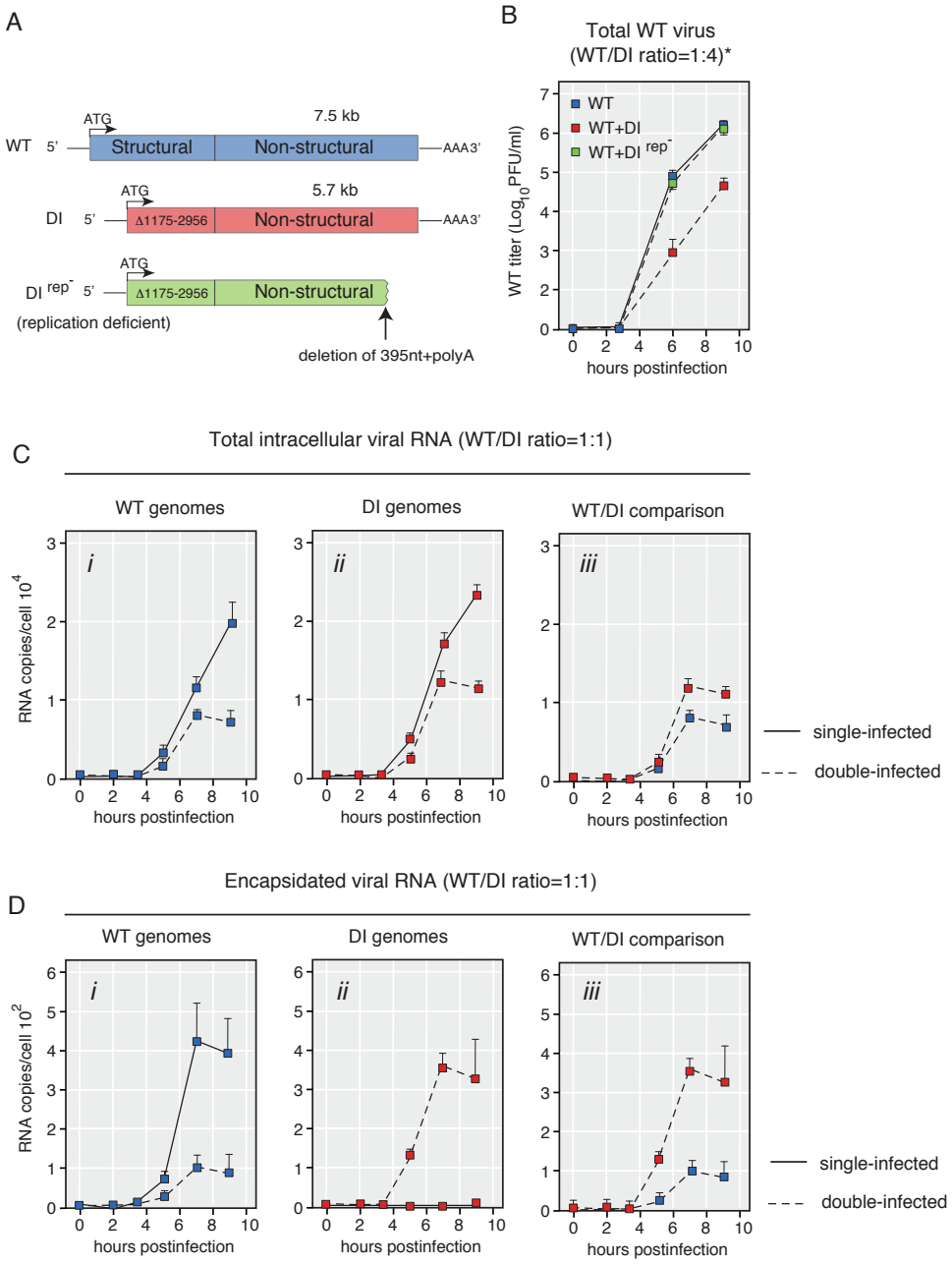

Figure 1: **DI genomes inhibit WT virus production via genomic replication and encapsidation.** (A) Structure of the WT poliovirus, DI(Δ1175-2956), and DI(Δ1175-2956)(Rep-). The DI genome has an in-frame deletion in its P1-encoding region. The PvuII-cut DI genome is used for a non-replicating RNA control (Rep-). (B) Growth curves of WT poliovirus after transfection of WT genomes and/or DI genomes (sampling time-points: 0, 3, 6 and 9 hours after transfection). (C, D) Copy numbers of total (C) or encapsidated (D) genomes over time after transfection (sampling time-points: 0, 2, 3.5, 5, 7 and 9 hours post transfection). Blue and red squares indicate copy numbers of WT and DI genomes, respectively. Solid lines indicate single-transfected (WT or DI genome-transfected) samples, while dotted lines indicate double-transfected (both WT and DI genomes-transfected) samples. n=3, mean ± standard deviations (SD) (B-D).

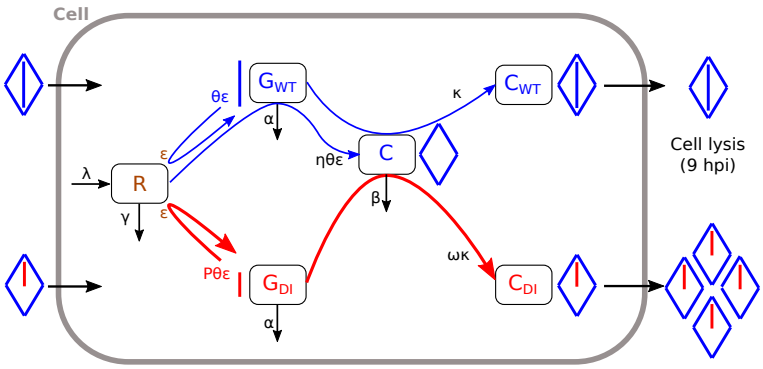

Figure 2: **Flow diagram of the model (Eqs.** (1)–(6)**).** State variables: resource units number R; wild-type (WT) poliovirus naked genome number G_{WT}; defective interfering (DI) naked genome number G_{DI}; WT-produced capsid proteins number C; encapsidated WT genome number C_{WT}; encapsidated DI genome number C_{WT}. Model parameters are defined in Table 1. Color code is blue for WT, red for DI and brown for resources. Segments represent genomes and diamonds represent capids.

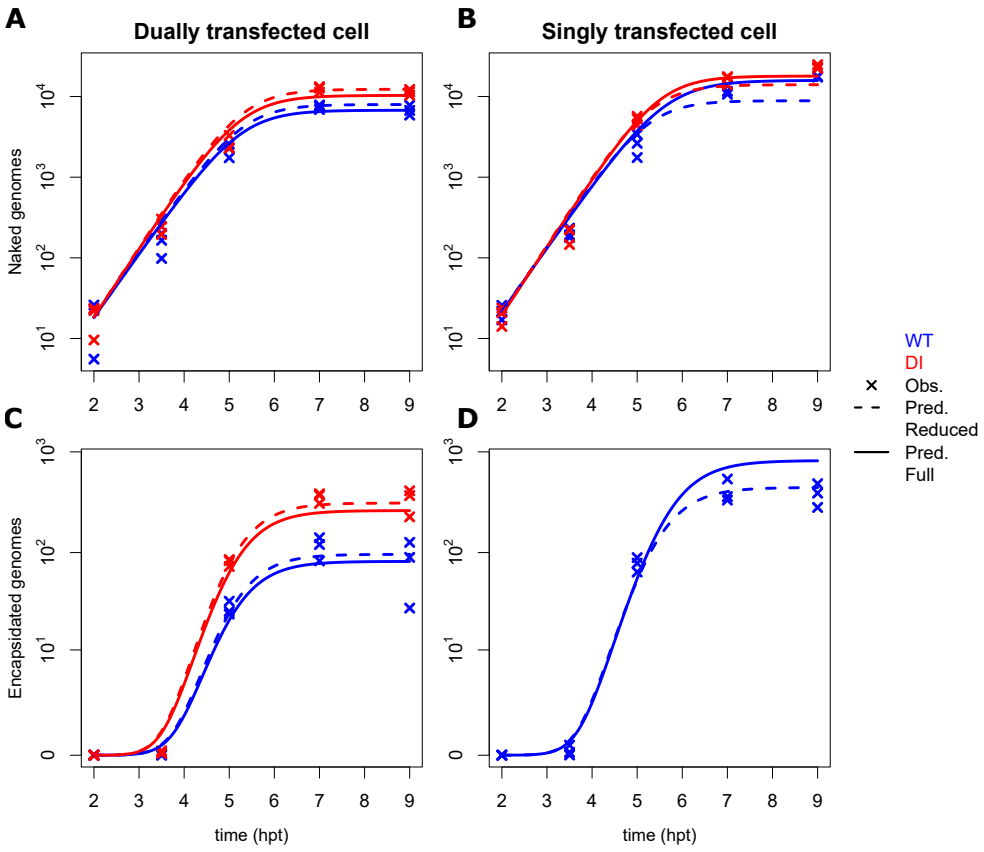

Figure 3: **Experimental data and model predictions for the naked and encapsidated wild-type (WT) and defective interfering (DI) genomes.** Evolution of the number of WT and DI (A-B) naked genome copies and (C-D) encapsidated genome copies with time, from 2 to 9 hours post transfection (hpt). (A & C) show data in dually infected cells whereas (B & D) show data in singly infected cells. WT and DI results are shown in blue and red color, respectively. Crosses indicate experimental data for 3 replicates per sampling time at 2, 3.5, 5, 7 and 9 hpt. Dashed curves represent the fit of the reduced model with logistic equation and solid curves show the fit of the full model (Eqs. (1)– (6)).

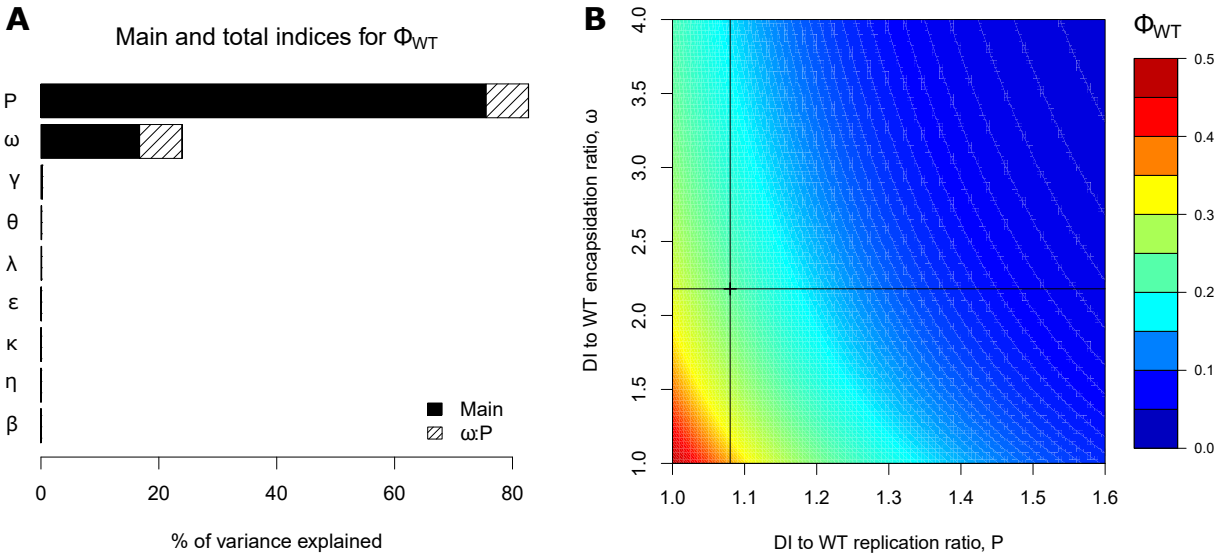

Figure 4: **Sensitivity indices for the proportion of WT virions at cell lysis (Φ_{WT}) and the impact of the most important parameters.** A: Main, total and most important interaction indices for Φ_{WT}. Main indices correspond to single parameter effect (black parts), and total indices add the effect of the factor in interaction with all other factors (second-order interactions, full bars). Hatched areas represent the importance of the strongest pairwise interaction between defective interfering (DI) to WT encapsidation rate ω and DI to WT replication factor P. B: Heat map representing the impact of P and ω on Φ_{WT}, all other parameters being fixed to their best estimated value. The cross and lines in (B) show estimated parameter values from fitting the model to the experimental data.

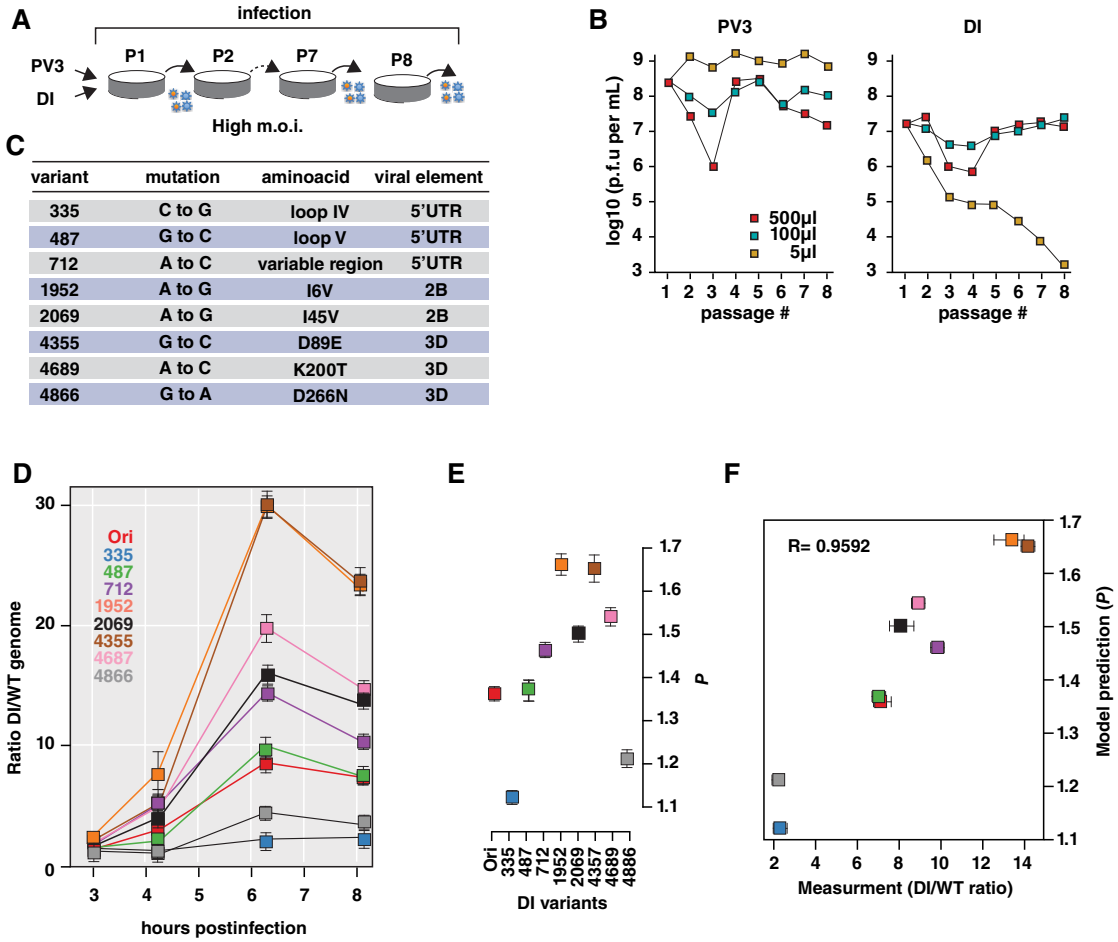

C

variant	mutation	aminoacid	viral element
335	C to G	loop IV	5'UTR
487	G to C	loop V	5'UTR
712	A to C	variable region	5'UTR
1952	A to G	I6V	2B
2069	A to G	I45V	2B
4355	G to C	D89E	3D
4689	A to C	K200T	3D
4866	G to A	D266N	3D

Figure 5: **Investigating DI mutant genomes.** A: PV3 and DI particles were serially passaged 8 times. B: Titers of PV3 (PFU/mL) and DI particles (IU/mL) included in the samples were determined. C: Mutations in the DI genomes positively selected over passages. D: One-step replication cycle. Dynamics of the ratio of DI to (wild-type) WT naked genome copies (total RNA) over time (3, 4.33, 6.33 and 8.17 hours post transfection), for distinct DI mutants (Ori: original non-mutant DI genome). E: Estimation of the ratio of DI to WT replication rate P from a least square regression between experimental and model predicted DI to WT naked genome ratios. Confidence intervals represent p–values at 10% of the minimum least square value. F: Model predictions of P against experimental DI to WT naked genome ratios at the last sampling time-point.

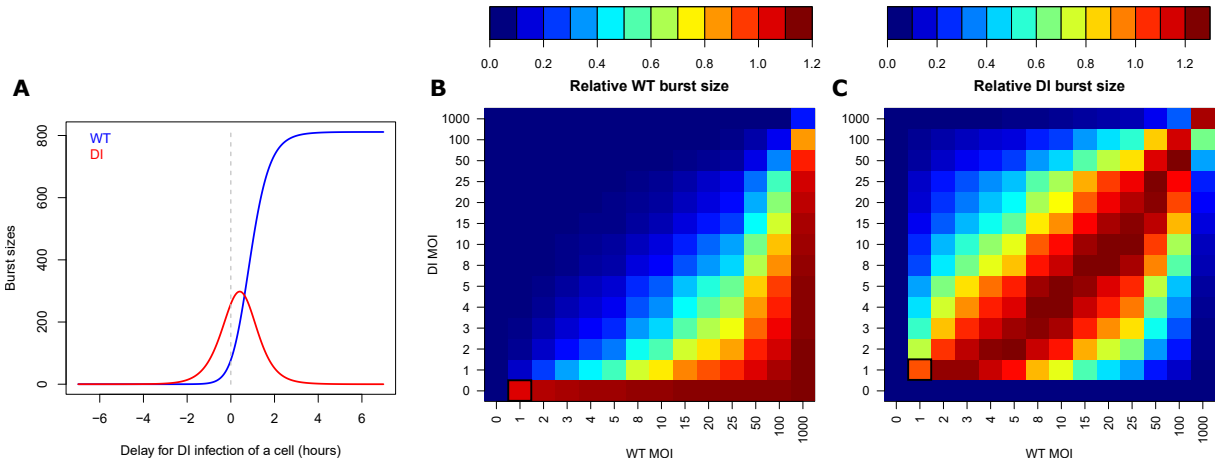

Figure 6: **Impact of infection delay and initial multiplicity of infection (MOI) on WT and DI burst sizes.** A: WT (blue) and DI (red) burst sizes (encapsidated genomes at 9 hours post infection) for various delays in DI infection of a cell. Negative delays correspond to cases where DI infects first and positive delays to cases where WT infects first. The dashed gray line marks the case of simultaneous infection by WT and DI. B-C: Heat maps representing the relative burst sizes of (B) WT, $\mathcal{B}_{WT}$, and (C) DI, $\mathcal{B}_{DI}$, as a function of initial WT (x-axis) and DI (y-axis) MOIs (input). WT burst sizes were normalized by WT burst size resulting from WT:DI = 1:0 MOIs and DI burst sizes by DI burst size resulting from WT:DI = 1:1 MOIs (black squares).

Table 1: Notations used in the model and model parameters.

Notation	Definition	Unit[a]			
	Observed variables				
g_{WT}^{tot}, g_{DI}^{tot}	WT, DI total genome number	gen			
v_{WT}, v_{DI}	WT, DI virion number	gen			
	State variables				
G_{WT}, G_{DI}	WT, DI genome number	gen			
C	Free capsid number	caps			
R	Resource units	uor			
C_{WT}, C_{DI}	WT, DI virion number	gen			
	Model parameters		**Best value**[c]	**Confidence Interval**[d]	**Sensitivity analysis**
c_g	Number of viral genomes per capsid	gen·caps^{-1}	1[b]		
c_r	Number of uor per viral genome	uor·gen^{-1}	1[b]		
θ	Genome replication factor	-	1.192	[1.000; 1.211]	[1, 1.25, 1.5, 1.75, 2]
ε	Resource capture rate by viral genomes	(uor·min)$^{-1}$	$1.814 \cdot 10^{-6}$	$[1.813; 1.814]\times10^{-6}$	$[0.8, 1.3, 1.8, 2.3, 2.8]\times10^{-6}$
κ	Encapsidation rate	(gen·min)$^{-1}$	$5.097 \cdot 10^{-6}$	$[4.900; 5.282]\times10^{-6}$	$[2, 3.5, 5, 6.5, 8]\times10^{-6}$
α	Viral genome decay rate	min^{-1}	0	-	0
η	Capsid to genome accumulation ratio	caps·gen^{-1}	$5.260 \cdot 10^{-2}$	$[5.058; 5.439]\times10^{-2}$	$[2, 3.5, 5, 6.5, 8]\times10^{-2}$
β	Capsid decay rate	min^{-1}	$2.589 \cdot 10^{-3}$	$[1.659; 3.476]\times10^{-3}$	$[1, 1.75, 2.5, 3.25, 4]\times10^{-3}$
P	DI-to-WT replication ratio	-	1.075	[1.062; 1.087]	[1, 1.15, 1.3, 1.45, 1.6]
ω	DI-to-WT encapsidation ratio	-	2.185	[1.943; 2.453]	[1, 1.75, 2.5, 3.25, 4]
λ	Resource production rate	uor·min^{-1}	$1.000 \cdot 10^{-3}$	$[1.000; 1.101]\times10^{-3}$	$[1, 1.25, 1.5, 1.75, 2]\times10^{-3}$
γ	Resource decay rate	min^{-1}	$7.157 \cdot 10^{-8}$	$[6.004; 7.273]\times10^{-8}$	$[3.5, 5.25, 7, 8.75, 10.5]\times10^{-8}$
L	Logistic's maximum	-	$3.078 \cdot 10^{-2}$	$[3.061; 3.099]\times10^{-2}$	-
s	Logistic's steepness	-	$-3.234 \cdot 10^{-2}$	$[-3.234; -3.234]\times10^{-2}$	-
t_0	Logistic's midpoint	min	318.459	[318.459; 318.459]	-

[a] gen: genome; caps: capsid; uor: unit of limiting resource; '-': dimensionless
[b] Fixed parameter values
[c] Best optimized value shared by the 85 first sets (identical until fourth significant digits) for reduced model optimization (P, ω, κ, η, α, β, L, s, t_0), and arbitrarily chosen best set for full model optimization (ε, θ, λ, γ).
[d] Range of variation over 150 best sets of parameter values

Supplementary Material

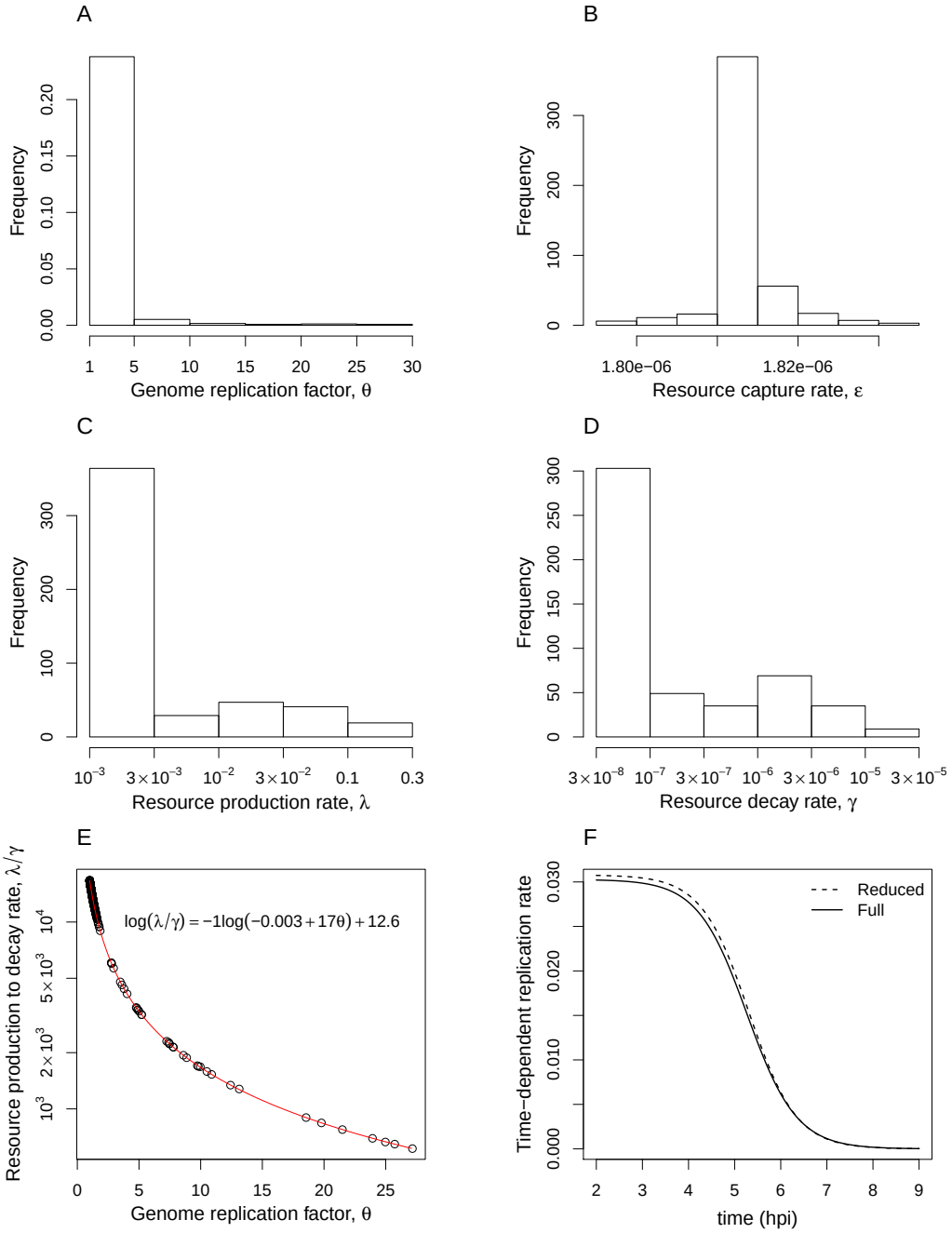

Figure S1: **Histograms and correlations of the genome replication factor (θ), the resource linear production (λ), the decay rate (γ), and the resource capture rate (ε).** The best 123 estimated values for each parameter are represented. A-D: Histograms of best estimated values for θ (A), ε (B), λ (C) and γ (D). E: Correlation between resource production to decay rate and genome replication factor. The best fit curve is shown in red and its equation is provided (Pearson p-value $< 2.2 \cdot 10^{-16}$ and $R^2 = 1$). F: Time-dependent replication rate given by the reduced model (Λ (t), dashed line) and the full model ($\theta\varepsilon R(t)$, plain line).

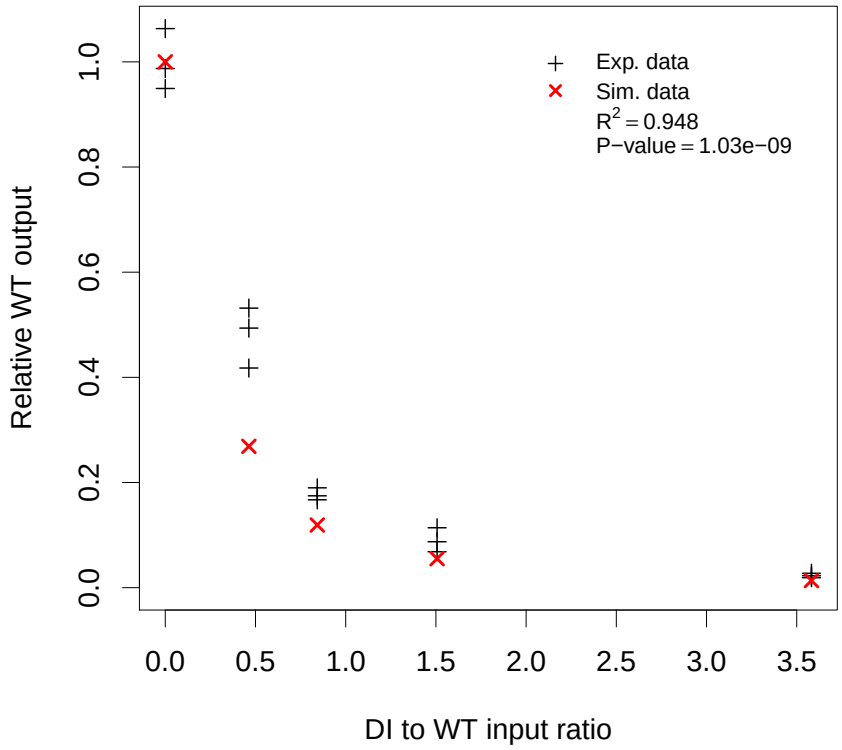

Figure S2: **Cross-validation of the model (Eqs.** (1)– (6)**).** Three experimental replicate values (black dots) of relative WT virus output are represented for various DI to WT input (proxy of multiplicities of infection) ratios. Red dots indicate predicted relative WT output starting with the same experimental input ratios. Experimental WT output corresponds to PFU while simulated WT output corresponds to burst size (number of encapsidated genomes at 9 hours post infection). All outputs were normalized by the output value (or the mean for experimental data) of WT:DI = 1:0 input ratio. R-squared and p-value of a Pearson correlation test between experimental and predicted WT outputs are given in the graphic.

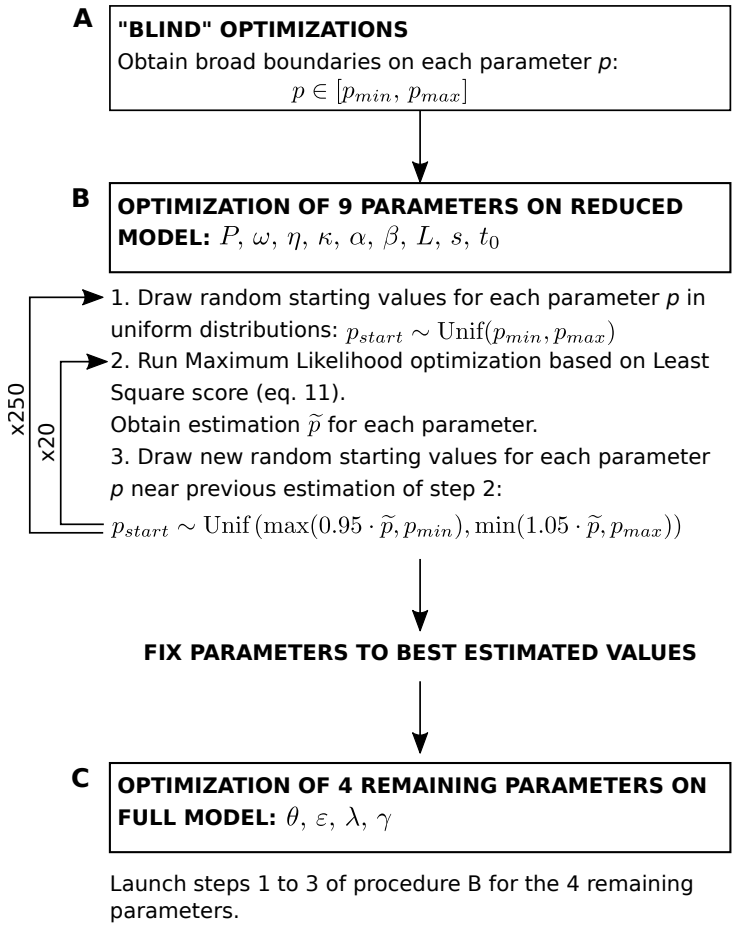

Figure S3: **Diagram of the parameter fitting procedure.**

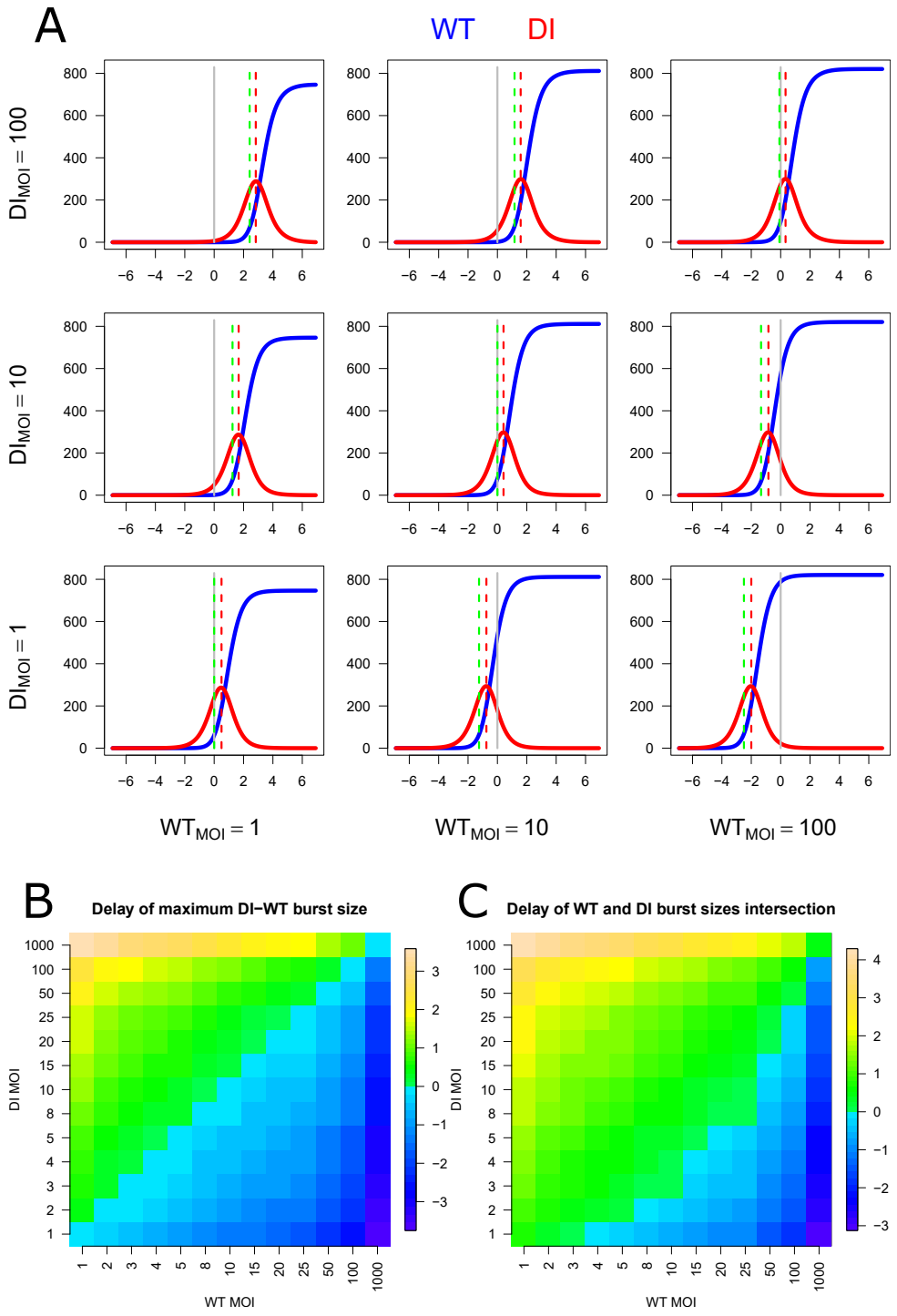

Figure S4: **Delay at various multiplicities of infection (MOIs).** A: Impact of delay for DI particle infection of a cell (x-axis, in hours) on WT (blue) and DI (red) burst sizes (y-axis). One line represents one DI MOI and one column one WT MOI. The grey vertical line indicates no-delay (simultaneous infection). The red vertical line indicates the peak of DI burst size and the green vertical line the maximum difference of DI to WT burst size. B: Heat map of the delay for the maximum difference of DI to WT burst size (green lines in A). C: Heat map of the delay for WT and DI burst size curves intersection.

Model	R^2	$-\mathbf{2 \cdot \log(L)}$	**AIC**
$\mathcal{M}^{\emptyset}$	0.717	-69.670	-63.670
$\mathcal{M}^{2}$	0.760	-83.567	-77.567
$\mathcal{M}^{23}$	0.760	-83.664	-77.664
$\mathcal{M}^{12L}$	0.970	-257.340	-251.340
$\mathcal{M}^{12}$	0.957	-227.307	-221.307
$\mathcal{M}^{123L}$	0.974	-268.831	-262.831
$\mathcal{M}^{123}$	0.965	-244.934	-238.934

Table S1: **Model selection.** For each model, described in Supplementary Methods, the goodness of fit is evaluated by the squared Pearson correlation coefficient between experimental and fitted data (R^2), and the quality of the models is evaluated by the log-likelihood ($-2 \cdot \log(L)$) and Akaike information criterion (AIC) from a linear model between experimental and fitted data.

Supplementary Methods

In this Supplementary Methods, we first describe the model selection procedure. We start by presenting the different models tested and then the statistics used to compare their goodness of fit and quality. In the second section, we describe how we estimated the ratio of DI to WT replication rate (P parameter) on the DI mutants experimental data.

Model selection procedure

Description of the models

We built different versions of our model based on the three main features that we hypothesized: (1) the replication and capsid production relies on limiting resources; (2) DI genomes replicate faster than WT genomes; and (3) DI genomes encapsidate faster than WT genomes.

Let us denote the full version of the model, including all three features and presented in the main text (Eqs. (1)– (6)), as $\mathcal{M}^{123}$, and its reduced version, assuming a logistic function for the decrease in resources (Eqs. (7)– (10)), as $\mathcal{M}^{123L}$. Now let us build a series of models lacking some of these features. We start with the simplest model, lacking all three features and denoted $\mathcal{M}^{\emptyset}$. The equations of $\mathcal{M}^{\emptyset}$ are:

$$\frac{dG_{WT}}{dt} = \zeta G_{WT} - c_g \kappa C G_{WT} - \alpha G_{WT} \quad (13)$$

$$\frac{dC}{dt} = \eta \zeta G_{WT} - \kappa (G_{WT} + G_{DI}) C - \beta C \quad (14)$$

$$\frac{dG_{DI}}{dt} = \zeta G_{DI} - c_g \kappa C G_{DI} - \alpha G_{DI} \quad (15)$$

This model has 5 parameters and is the most basic, with a similar replication rate for WT and DI genomes ζ, a ratio of capsid to genome production by WT η, a similar encapsidation rate for WT and DI genomes κ, and a decay rate of genomes (resp. capsids) α (resp. β).

We now introduce the most obvious feature: the faster replication of DI genomes, based on their shorter size [29]. The model is denoted $\mathcal{M}^{2}$ and reads as:

$$\frac{dG_{WT}}{dt} = \zeta G_{WT} - c_g \kappa C G_{WT} - \alpha G_{WT} \quad (16)$$
$$\frac{dC}{dt} = \eta\zeta G_{WT} - \kappa(G_{WT} + G_{DI})C - \beta C \quad (17)$$
$$\frac{dG_{DI}}{dt} = P\zeta G_{DI} - c_g \kappa C G_{DI} - \alpha G_{DI} \quad (18)$$

The only additional parameter is P, representing the ratio of DI to WT replication rate, appearing in the equation for DI genomes (G_{DI}). Next, we add either of the two other features to this model. Model $\mathcal{M}^{23}$ assumes both the faster replication (feature 2) and encapsidation (feature 3) of DI genomes:

$$\frac{dG_{WT}}{dt} = \zeta G_{WT} - c_g \kappa C G_{WT} - \alpha G_{WT} \quad (19)$$
$$\frac{dC}{dt} = \eta\zeta G_{WT} - \kappa(G_{WT} + \omega G_{DI})C - \beta C \quad (20)$$
$$\frac{dG_{DI}}{dt} = P\zeta G_{DI} - c_g \omega \kappa C G_{DI} - \alpha G_{DI} \quad (21)$$

It has one additional parameter, ω, representing the ratio of DI to WT encapsidation rate. Finally, model $\mathcal{M}^{12}$ assumes that DI genomes replicate faster than WT genomes (feature 2), and that replication and capsid production rely on limiting resources (feature 1):

$$\frac{dG_{WT}}{dt} = \theta\varepsilon G_{WT} R - c_g \kappa C G_{WT} - \alpha G_{WT} \quad (22)$$
$$\frac{dC}{dt} = \eta\theta\varepsilon G_{WT} R - \kappa(G_{WT} + G_{DI})C - \beta C \quad (23)$$
$$\frac{dG_{DI}}{dt} = P\theta\varepsilon G_{DI} R - c_g \kappa C G_{DI} - \alpha G_{DI} \quad (24)$$
$$\frac{dR}{dt} = \lambda - c_r \varepsilon (G_{WT} + G_{DI})R - \gamma R \qquad R(0) = \lambda/\gamma \quad (25)$$

This model has a total of 9 parameters and one new state variable for the resources that are depleted during replication and capsid production. The new parameters are the genome replication factor θ, the resource capture rate by viral genomes ε, the resource production rate λ and the resource decay rate γ. We can link parameter ζ of the previous models relaxing the assumption of feature 1 (the presence of limiting resources required for

replication and capsid production) to the parameters of this last model $\mathcal{M}^{12}$ including this feature, by noting that at time t=0: $\zeta = \theta\varepsilon R(0) = \theta\varepsilon\lambda/\gamma$. As for the full model including the three features $\mathcal{M}^{123}$ presented in the main text, we can build a lower dimension version of model $\mathcal{M}^{12}$ by assuming that the decrease in resources due to viral uptake for replication and capsid production follows a logistic decreasing function. The reduced model, denoted $\mathcal{M}^{12L}$, reads as:

$$\frac{dG_{WT}}{dt} = \Lambda(t)G_{WT} - c_g\kappa CG_{WT} - \alpha G_{WT} \quad (26)$$

$$\frac{dC}{dt} = \eta\Lambda(t)G_{WT} - \kappa(G_{WT} + G_{DI})C - \beta C \quad (27)$$

$$\frac{dG_{DI}}{dt} = P\Lambda(t)G_{DI} - c_g\kappa CG_{DI} - \alpha G_{DI} \quad (28)$$

$$\Lambda(t) = \frac{L}{1 + e^{-s(t-t_0)}} \quad (29)$$

Optimization and comparison of the models

The optimization of each model was conducted iteratively, as described in the main text. Models $\mathcal{M}^{\emptyset}$, $\mathcal{M}^{2}$ and $\mathcal{M}^{23}$ were optimized in one step (20 times 250 optimizations), whereas model $\mathcal{M}^{12}$ was optimized in two steps, first estimating the parameters of reduced model $\mathcal{M}^{12L}$, and then fixing the common parameters between the two models (κ, α, β, P) to estimate the remaining parameters of model $\mathcal{M}^{12}$ in a second step (θ, ε, λ, γ).

For each model, the 150 best optimized sets of parameters were retained and used to compute the squared Pearson correlation coefficient between experimental and fitted data (R^2), and the log-likelihood ($-2\cdot\log(L)$) and Akaike information criterion (AIC) of a linear model between experimental and fitted data. The values of these statistics are presented in Table S1. Although two versions of the model ($\mathcal{M}^{12L}$ and our reduced model $\mathcal{M}^{123L}$) were predicted to perform slightly better than our full model ($\mathcal{M}^{123}$, Eqs. (1)– (6)) based on tested statistics, we decided to keep our full model because it visually fits better the experimental data, reproducing its most important characteristics. Additionally, its statistics are very good.

Analysis of DI mutants

Passaging experiment

A PV1-DI construct encoding the Venus (a green fluorescent protein) gene in place of the P1 gene was used for the following experiments. We transfected 5μg of PV3 and 1.25μg of PV1-DI genomes, and collected viruses at 24 hours after transfection as the passage 1 (P1) sample. Then, 1.0×10^6 HeLaS3 cells were infected with the different amounts of the P1 sample (500, 100, and 5 μl), and collected 24 hours after infection. The virus samples were passaged 8 times in the same manner. Viral RNAs for each sample were then analyzed by CirSeq [40] to identify accumulated mutations in DI.

Competition experiment and analysis

An additional experiment was conducted on eight DI mutants and the parental PV1-DI construct encoding the Venus gene. To obtain DI particles for the experiments, a packaging cell line was established. HeLaS3 cells were transfected with a pcDNA4 plasmid encoding the PV1 P1 (capsid) gene, followed by selection with Zeocin. We used a clone stably expressing P1 proteins (HeLaS3/P1) to generate DI particles. HeLaS3/P1 cells were transfected with DI RNAs by electroporation, and DI particles were collected 24 hours after transfection. Each of the DI variant was put in competition with the WT virus, and the number of naked genome copies was measured at 3, 4.33, 6.33 and 8.17 hours post transfection, with three replicates per time-point. Only the ratio of DI-to-WT naked genome copies is kept for further analysis.

We assumed that the mutations only affect the replication of each DI variant, hence we set all model parameters to their best estimated values (see Table 1) except for the DI-to-WT replication ratio P that we varied between 1 and 1.8. We set the initial conditions to 10 copies of DI and WT (each) naked genomes at 2 hours post transfection. We assumed that there was initially no capsids or encapsidated genomes, and the number of resource units was set as in the main experiment to λ/γ. We recorded the numbers of DI and WT naked genome copies at the experimental time-points for varying values of P (step of 0.01). The best P value for each DI variant was found as the one minimizing the sum of the least square difference between experimental and simulated ratio of DI-to-WT naked genome copies.